

Spatial control and cell guidance in evolving biological tissues

Solene Hegarty-Cremer

Bachelor of Mathematics (QUT), 2018

A dissertation submitted in fulfilment of the
requirement for the degree of
Master of Philosophy

Supervised by

Dr Pascal Buerzli and Prof. Matthew Simpson



School of Mathematical Sciences
Science and Engineering Faculty
Queensland University of Technology
Australia
2020

Keywords: mathematical biology, computational modelling, tissue growth,
bone remodelling, tissue engineering, moving boundary problems,
experimental data

Statement of Authorship

In accordance with the requirements of the degree of Master of Philosophy in the School of Mathematical Sciences, Faculty of Science and Engineering, I present the following thesis entitled,

Spatial control and cell guidance in evolving biological tissues.

This work was performed under the supervision of Dr. Pascal Buenzli and Prof. Matthew Simpson. I declare that the work submitted in this thesis is my own, except as acknowledged in the text, and has not been previously submitted for a degree at Queensland University of Technology or any other institution.

Signed,



Solene Hegarty-Cremer

26 August 2020

Acknowledgements

I firstly want to thank my primary supervisor, Pascal Buerzli. Thank you for your detailed and insightful feedback and always being willing to discuss the project when needed. Your guidance, support, and encouragement throughout this thesis have been greatly appreciated.

My thanks also go to my co-supervisor, Matthew Simpson, for your technical support and guidance and the ideas that came from our weekly discussions. I would also like to thank our collaborators, Thomas Andersen, Christian Andreasen, and Xenia Bolgaard for providing us with experimental data and the discussing the biological background of our work.

I want to thank and acknowledge the financial support from the Australian Mathematical Sciences Institute, the School of Mathematics, and the Institute of Health and Biological Innovation. I am grateful to have been able to present my work at QANZIAM 2019 and at ANZIAM 2020.

I also thank my fellow research students, in particular Tamara and Ryan who helped me work through problems and offered support. I also want to thank the QUT Counselling Services, who provided guidance as I was navigating research for the first time. Finally, I want to thank my family and friends for encouraging me to have confidence in my work.

Abstract

Tissue geometry is an important influence on the evolution of many biological tissues. The local curvature of an evolving tissue induces cell crowding or spreading, which leads to differential tissue growth rates, and to changes in cellular tension, which can influence cell behaviour. In this thesis, a cell-based mathematical model for the curvature control of evolving biological tissues is presented to investigate how this control mechanism interacts with directed cell guidance mechanisms. First, the mathematical model is derived from conservation principles applied to the density of tissue synthesising cells at or near the tissue's moving boundary. The resulting partial differential equation is then solved numerically using a hybrid front-tracking method called the cell-based particle method. We apply this model to understand how angled bone tissue formation may generate anisotropies in tissue material properties, and to understand the role of tangential cell motion in the bone resorption process. Finally, ongoing work is presented on the application of the model to experimental bone pore infilling data available through collaboration with experimental bone biologists. This work involves exploring mechanisms which could cause irregular tissue growth behaviour in bone, where the infilling of bone pores is asymmetric.

Contents

1	Introduction	1
2	Modelling cell guidance and curvature control in evolving biological tissues	5
1	Introduction	9
2	Description of the model	13
2.1	Numerical method	20
3	Results	21
3.1	Validation of the numerical method	21
3.2	Circular bone pore infilling	24
3.3	Bone resorption in basic multicellular units	26
4	Discussion and conclusion	30
2.A	Evolution of local surface area	34
2.B	Comparison with the literature	35
2.C	Numerical Discretisation	36
2.D	Effect of resorption constants	39
3	Experimental Data Study	42
1	Introduction	42
2	Experimental Data	44
3	Methods	45
3.1	Mathematical model	46
3.2	Parameter Sweep	48

4	Results	55
4.1	Osteons with off-center Haversian canals	60
4.2	Numerical solver issues	63
4.3	Discussion	65
4	Concluding Remarks and Outlook	67

Chapter 1

Introduction

Understanding the evolution of biological tissues is important to tissue engineering and regenerative medicine, where the controls which govern new tissue growth need to be manipulated (Dzobo et al., 2018; Ambrosi et al., 2019). The understanding of tissue evolution is also important in developmental biology, where the question of how organisms manage remodelling and growth is critical (Goriely, 2017). However, in many biological situations, tissue growth cannot be observed within the living organism (*in vivo*) and further, in some situations the growth cannot be observed in laboratory settings (*in vitro*) either. Mathematical models for the evolution of tissues can be used to connect the different data obtained experimentally including information about tissue geometry and cell density (Rumpler et al., 2008; Alias and Buenzli, 2017; McCue et al., 2019). This data often comes in the form of frozen snapshots of the tissue in time. Tissue growth in bioscaffold infilling, tumour growth, wound healing, and bone pore infilling are all examples where mathematical modelling has been used to gain insights into the evolution of tissues (Figure 1.1) (Maini et al., 2004; Lowengrub et al., 2010; Kollmannsberger et al., 2011; Bidan et al., 2012, 2013; Guyot et al., 2014; Jin et al., 2018; Alias and Buenzli, 2018). Furthermore, mathematical models provide methods to link experimentally observed tissue behaviour with individual cell activity. This is achieved by making assumptions about cell behaviour, which may not be observable experimentally, and testing biological

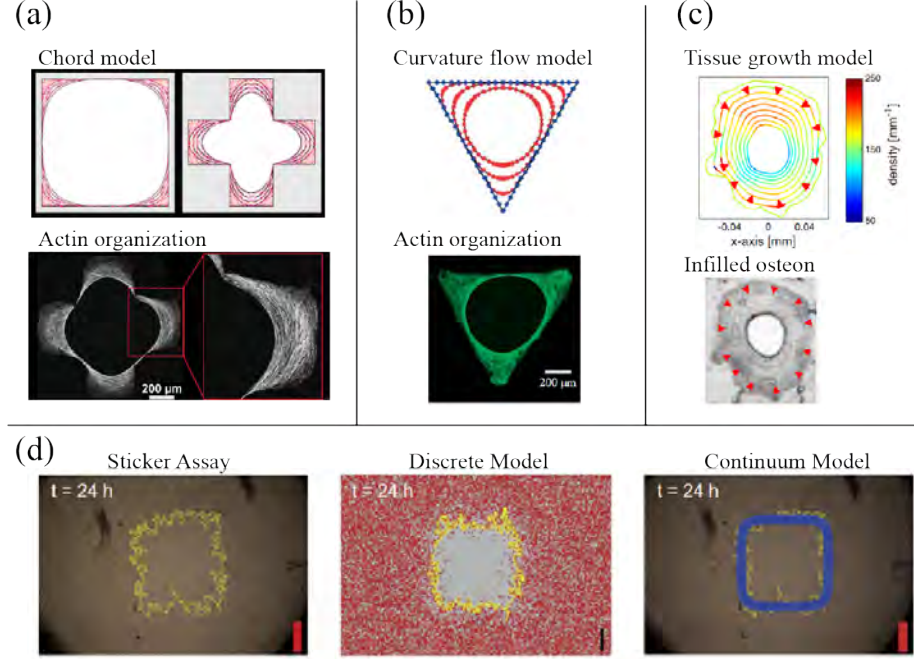


Figure 1.1: Mathematical models can be used to reflect experimentally observed tissue evolution behaviour and gain insights into cell behaviour. (a) Curvature control model where tissue growth is described by the assembly of tensile elements, chords. The output of the model (top) reflects the actin organization of the experimental data of bioscaffold infilling (bottom), reproduced with permissions from [Bidan et al. \(2013\)](#). (b) Mean curvature flow models (top) can be used to describe the infilling of different geometries of bioscaffolds (bottom), reproduced with permissions from [Rumpler et al. \(2008\)](#). (c) Tissue growth models derived from cell conservation principles (top) reflect the behaviour observed in experimental data of osteon (bone pore) infilling (bottom), reproduced with permissions from [Alias and Buenzli \(2018\)](#). (d) Wound healing in different geometries can be modelled using mathematical discrete and continuum models, reproduced with permissions from [Jin et al. \(2018\)](#)

hypotheses using the mathematical models ([Rumpler et al., 2008](#); [Bidan et al., 2013](#); [Guyot et al., 2014](#); [Alias and Buenzli, 2017](#); [Buenzli et al., 2020](#)).

The rate of tissue growth has been shown to depend on tissue geometry, more specifically on the local curvature of the underlying tissue ([Rumpler et al., 2008](#); [Bidan et al., 2012](#); [Ehrig et al., 2019](#)). This dependence of tissue growth rate on

curvature can be modelled using curvature flows. Curvature flow models have been quantitatively compared to experimental bioscaffold pore infilling data and have been shown to accurately reflect infilling behaviour as well as answer questions about the most efficient infilling pore shape and size (Rumpler et al., 2008; Bidan et al., 2013; Guyot et al., 2014; Ehrig et al., 2019; Alias and Buenzli, 2019; Buenzli et al., 2020).

In this thesis, a mathematical model is developed for tissues that evolve under curvature control and that are affected by cell guidance mechanisms. Cell guidance mechanisms consist of signals which pull cells in a particular direction and can be caused by chemical cues, mechanical cues, or other physical cues in the environment. Our mathematical model is used to explore new biological applications where directed cell guidance is needed to explain observed patterns of tissue growth. A concrete application of the model to bone pore infilling is presented, where specific experimental data available through collaboration enables us to illustrate how mathematical models can be used to test hypotheses about cell behaviours that cannot be observed directly.

The thesis is structured as follows. Chapter 2 consists of a journal article submitted to the Journal of Theoretical Biology and available as a preprint (Hegarty-Cremer et al., 2020). In Chapter 2, the model of tissue growth subject to curvature control and directed cell guidance mechanisms is derived in three dimensional, covariant form from rigorous conservation principles. This is achieved by considering the conservation of cells on an evolving surface. This model is compared to similar models from the literature. A hybrid front-tracking method, the cell-based particle method, is implemented to solve the model (Leung and Zhao, 2009; Leung et al., 2011; Hon et al., 2014). Then, two applications

of interest are considered: (i) the generation of anisotropies in tissue material properties during bone pore infilling; and (ii) hypothesis testing of cell guidance mechanisms required for the model to retrieve observed patterns of bone resorption.

In Chapter 3, the model is applied to experimental data on the infilling of bone pores, called osteons (Martin et al., 2004). A quantitative comparison framework is devised to find optimal model parameters for experimental data on osteons being infilled. Once the suitability of the model to osteon infilling is established, the model is then used to assess hypotheses about the formation of atypical osteons. This example illustrates the benefits of the mathematical model for answering questions about the development of biological tissues which may not be addressable experimentally. For example, the movement and secretion rate of individual bone-secreting cells cannot currently be measured, but can be included in the mathematical model. The model helps us interpret the signatures that may be visible experimentally in tissue samples as traces of specific cell behaviours. This allows us to identify requirements for new experimental data to be collected, which is part of ongoing work with our collaborators. The thesis is then concluded with an outlook on possible future research areas.

Chapter 2

Modelling cell guidance and curvature control in evolving biological tissues

This chapter contains the manuscript submitted for publication to the Journal of Theoretical Biology which is available as a preprint, ([Hegarty-Cremer et al., 2020](#)). The statements of contribution are included in the next page.

Title: Modelling cell guidance and curvature control in evolving biological tissues

Authors: Hegarty-Cremer^a, S.G.D., Simpson, M. J.^a, Andersen, T.L.^{b,c,d}, and Buenzli, P.R.^a

Affiliations:

a: School of Mathematical Sciences, Queensland University of Technology (QUT), Brisbane, Australia.

b: Clinical Cell Biology, Department of Pathology, Odense University Hospital, Odense, Denmark.

c: Pathology Research Unit, Department of Clinical Research, University of Southern Denmark, Odense, Denmark.

d: Department of Forensic Medicine, Aarhus University, Aarhus, Denmark.

Publication Title:

Modelling cell guidance and curvature control in evolving biological tissues

Publication Status:

Submitted to Journal of Theoretical Biology.

Contributor	Statement of contribution*
Solene G.D. Hegarty-Cremer  Signature	Wrote manuscript, derived model and ran simulations, data analysis and figure generation
20/08/2020 Date	
Matthew J. Simpson Confirmed agreement via email Signature	Aided with model derivation and data analysis and reviewed manuscript.
DD/MM/2020 Date 20/08/2020	
Thomas L. Andersen  Signature	Reviewed manuscript and aided with conception of modelling biological factors of bone remodelling
20/08/2020 Date	
Pascal R. Buenzli  Signature	Conception of mathematical work and biological application, initial mathematical model, aided with computational solution, reviewed and edited manuscript
DD/MM/2020 Date 20/08/2020	

Principal Supervisor Confirmation

I have sighted email or other correspondence from all Co-authors confirming their certifying authorship. (If the Co-authors are not able to sign the form please forward their email or other correspondence confirming the certifying authorship to the GRC).



Name



Signature



Date

The authors listed above have certified that:

1. they meet the criteria for authorship and that they have participated in the conception, execution, or interpretation, of at least that part of the publication in their field of expertise;
2. they take public responsibility for their part of the publication, except for the responsible author who accepts overall responsibility for the publication;
3. there are no other authors of the publication according to these criteria;
4. potential conflicts of interest have been disclosed to (a) granting bodies, (b) the editor or publisher of journals or other publications, and (c) the head of the responsible academic unit, and
5. they agree to the use of the publication in the student's thesis and its publication on the [QUT's ePrints site](#) consistent with any limitations set by publisher requirements.

Abstract

Tissue geometry is an important influence on the evolution of many biological tissues. The local curvature of an evolving tissue induces tissue crowding or spreading, which leads to differential tissue growth rates, and to changes in cellular tension, which can influence cell behaviour. Here, we investigate how directed cell motion interacts with curvature control in evolving biological tissues. Directed cell motion is involved in the generation of angled tissue growth and anisotropic tissue material properties, such as tissue fibre orientation. We develop a new cell-based mathematical model of tissue growth that includes both curvature control and cell guidance mechanisms to investigate their interplay. The model is based on conservation principles applied to the density of tissue synthesising cells at or near the tissue's moving boundary. The resulting mathematical model is a partial differential equation for cell density on a moving boundary, which is solved numerically using a hybrid front-tracking method called the cell-based particle method. The inclusion of directed cell motion allows us to model new types of biological growth, where tangential cell motion is important for the evolution of the interface, or for the generation of anisotropic tissue properties. We illustrate such situations by applying the model to simulate both the resorption and infilling components of the bone remodelling process, and provide user-friendly MATLAB code to implement the algorithms.

1 Introduction

Understanding the mechanisms controlling the generation of biological tissue is an important challenge in biomechanics and mechanobiology (Ambrosi et al., 2019) with key applications in tissue engineering and developmental biology (O’Brien, 2011; Dzobo et al., 2018). Tissue geometry influences the generation of new tissue, particularly the rate of tissue growth and the organisation of tissue material (Curtis and Varde, 1964; Dunn and Heath, 1976; Kollmannsberger et al., 2011). Several tissue growth experiments show that the rate of tissue progression is strongly dependent on tissue curvature. These findings apply to bioscaffold pore infilling (Bidan et al., 2013, 2016; Guyot et al., 2014; Ripamonti and Roden, 2010), wound healing (Poujade et al., 2007; Rolli et al., 2012), tumour growth (Lowengrub et al., 2010), and bone remodelling (Martin, 2000; Alias and Buenzli, 2018). This proportionality of growth rate and curvature may be caused by the crowding and spreading of cells and tissue material due to spatial constraints, and curvature-dependent tissue surface tension influencing cell proliferation rates (Nelson et al., 2005; Rumpler et al., 2008; Haeger et al., 2015; Alias and Buenzli, 2017; Buenzli et al., 2020).

In addition to the collective influence of curvature on tissue progression, other factors such as mechanical or chemical cues in the environment as well as cell-scale geometrical features can induce individual cell responses including directed cell migration. Mechanical cues include viscoelasticity (Chaudhuri et al., 2016), surface stiffness (Pelham and Wang, 1997; Lo et al., 2000; Discher et al., 2005; Engler et al., 2006), or surface mechanical stretch (Trepaut et al., 2007; Livne et al., 2014). Chemical cues include signalling molecules inducing attractive or repulsive chemical gradients (Haeger et al., 2015), and cell-scale geometrical

cues include geometrical guidance such as curvotaxis (Callens et al., 2020) and surface roughness gradients (Martin et al., 1995; Deligianni et al., 2001). While the collective influence of curvature on tissue growth and the effects of environmental cues on cell guidance mechanisms are well studied in isolation, how these processes interact during the generation of new biological tissue remains poorly understood.

In this work we develop a new mathematical model which explicitly includes both the collective influence of curvature and directed cell guidance mechanisms. The addition of directed cell guidance allows us to model new types of biological growth, which cannot be generated by existing mathematical models where the tissue interface progresses in the normal direction only (Bidan et al., 2013; Guyot et al., 2014; Alias and Buenzli, 2017; Callens et al., 2020).

Indeed, the growth of several tissues involves directed cell motion where cells move tangentially along the tissue surface (Figure 2.1). For example, shells, horns, and tusks with a spiralling structure are generated by tissue being secreted at an angle to the base membrane (Figure 2.1a) (Skalak et al., 1982, 1997). Tangential cell velocity may also be responsible for the generation of anisotropies in tissue material properties by aligning tissue fibrils with respect to the cells motion (Figure 2.2). In lamellar bone, the so-called twisted plywood structure of collagen fibrils may be due to the osteoblasts (bone secreting cells) changing direction of motion during bone infilling (Martin et al., 2004) (Figure 2.1c). Finally, tangential cell motion is suspected to occur in bone resorption to keep osteoclasts at the front of the resorption cone (Figure 2.1c).

Mathematically, the evolution of *smooth* interfaces can be described by the

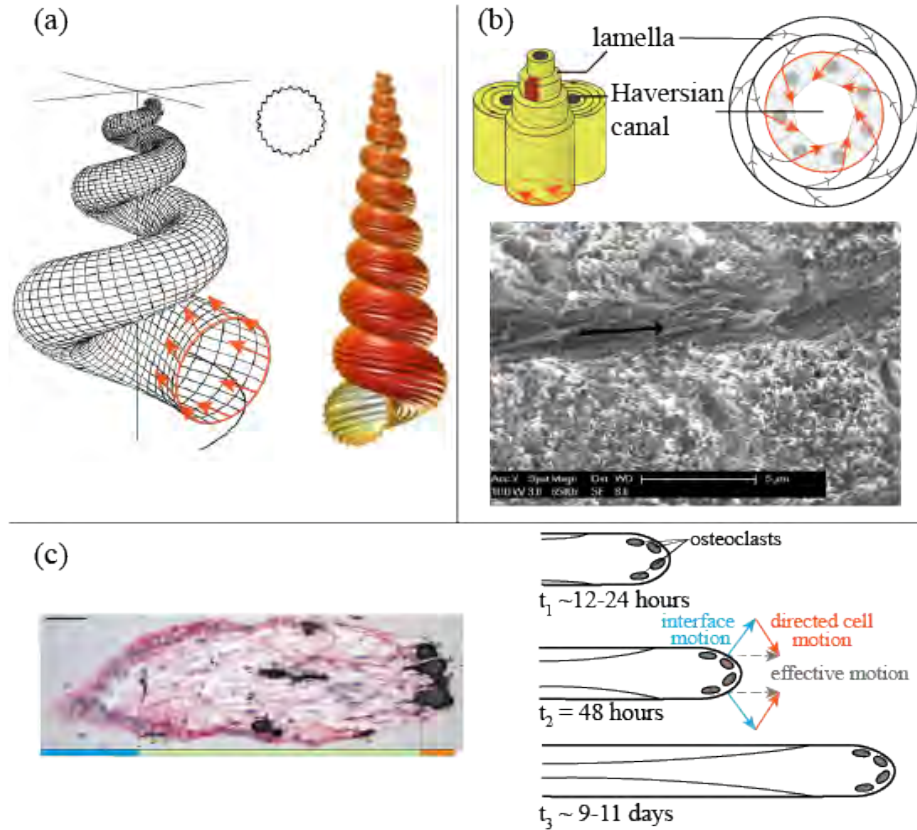


Figure 2.1: Tangential cell movement in tissue growth. (a) Shells grow by secretion of new tissue at their base (mantle) at an angle to create spiralling structures (reproduced with permissions from [Goriely \(2017\)](#)). (b) In lamellar bone, successive tissue layers possess different collagen fibril orientations which suggest changes in the tangential motion of osteoblasts during bone formation (reproduced with permissions from [Pazzaglia et al. \(2012\)](#) and [Schrof et al. \(2014\)](#)). (c) Resorption cavities during bone resorption maintain a stable resorption front shape at the tip. Since the dissolution process of bone by osteoclasts is expected to occur in the normal direction, this suggests osteoclasts are subject to cell guidance signals toward the cavity centerline. An example of the serial section of a cutting cone, immunostained (black) for an osteoclastic marker, obtained from [Lassen et al. \(2017\)](#) and schematic of an evolving Haversian system, after [Jaworski and Hooper \(1980\)](#).

normal velocity of the interface only ([Sethian, 1999](#)). However, biological tissue interfaces may develop cusps and sharp edges ([Skalak et al., 1997](#); [Alias and](#)

Buenzli, 2017; Goriely, 2017). When these move at an angle to their base, one is required to consider a more general tissue interface velocity that includes a tangential component to avoid the emergence of singularities in the governing equation for tissue growth velocity (Skalak et al., 1997).

Many existing models of geometric control of tissue growth consider the geometry of the tissue substrate only, so that cell guidance mechanisms and cell crowding effects are not modelled explicitly (Skalak et al., 1982, 1997; Rumpel et al., 2008; Bidan et al., 2012, 2013; Gamsjager, 2013; Guyot et al., 2014; Goriely, 2017; Ehrig et al., 2019). Here, we consider the cell-based mathematical model of Alias and Buenzli (2017), which explicitly accounts for curvature-induced cell crowding and spreading, and we generalise this model to allow for tangential cell motion. We derive the model from general conservation properties imposed on cells, which allows us to explicitly include cell behaviours. To our knowledge, no mathematical model currently includes both the effect of curvature on collective cell crowding and spreading and tangential cell motion mechanisms.

The model of Alias and Buenzli (2017) is also extended to three dimensions and the governing equations are derived in covariant form. The model derived is a partial differential equation (PDE) for the density of cells to be solved on a moving boundary, which represents the evolving tissue surface. This problem is numerically solved to explore several situations in which tangential cell guidance mechanisms are added. We demonstrate that with the addition of tangential cell advection, new biologically relevant tissue growth phenomena can be modelled, such as bone resorption and the generation of different fibre orientations in lamellar bone.

2 Description of the model

Tissue growth usually occurs by cells synthesising new tissue close to the tissue's interface. To determine general evolution equations for the density of tissue-synthesising cells subject to normal and tangential motion, we consider the case where the tissue-synthesising cells are attached to the tissue interface and described by a surface density, ρ (number of cells per unit surface). The motion of the interface transports the cells in space and the cells may additionally move laterally with respect to the material points of the surface. The motion of the interface is considered to be due to new tissue being synthesised in the wake of these surface-bound cells (Figure 2.2). This situation occurs for example in wound healing, bone remodelling, bioscaffold pore infilling, and tumour growth (Poujade et al., 2007; Rumpel et al., 2008; Lowengrub et al., 2010; Bidan et al., 2013; Guyot et al., 2014) where tissue-synthesising cells are located at or near the tissue interface. The normal velocity of the tissue interface, $u_n \mathbf{n}$ where \mathbf{n} is the outward-facing unit surface normal, is given by

$$u_n = k\rho, \quad (2.1)$$

where k is the tissue-synthesising cells' secretory rate (volume of new tissue synthesised per unit time per cell) (Buenzli, 2015). Tissue resorption can also be modelled by assuming k to be negative. During the evolution of the tissue, the interface may stretch locally depending on its curvature (Figure 2.2a), and this will induce changes in cell density. Convex areas of the tissue substrate result in cells spreading whereas concave areas of the tissue substrate result in cells crowding. In addition, cell guidance mechanisms superimpose lateral cell motion with respect to the tissue interface. Directional tissue growth may therefore result from a combination of interface motion and lateral cell motion

(Figures 2.2b and 2.3).

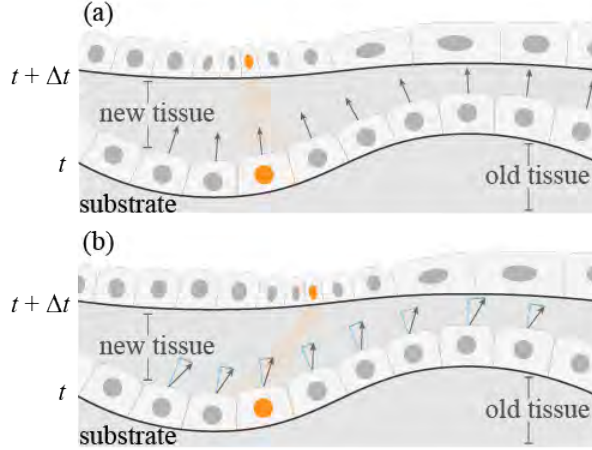


Figure 2.2: Schematic illustrating the crowding and spreading effect of curvature and the influence of tangential motion for tissue material properties; (a) shows only movement in the normal direction and the resulting changes in density; (b) includes both curvature control and cell guidance, meaning the cells crowd and spread and also undergo directed motion, creating anisotropies in tissue material properties (thin orange lines).

The tissue interface is denoted by $S(t)$ and $\rho(\mathbf{r}_S, t)$ denotes the surface density of the tissue-synthesising cells, at position \mathbf{r}_S on $S(t)$. We formally define $\rho(\mathbf{r}_S, t)$ by considering an infinitesimal element of surface δS at position \mathbf{r}_s of $S(t)$, and the number of cells living on this area, δN . It is important to choose δS small enough to capture heterogeneous densities but large enough to contain a sufficient number of cells to define a continuous surface density of cells, such that

$$\rho = \frac{\delta N}{\delta S}. \quad (2.2)$$

We now derive a conservation law for the surface density of cells living on the evolving surface as the tissue evolves. To do so, we consider the material derivative of ρ following the material trajectories, $\mathbf{r}_S(t)$, of the surface $S(t)$,

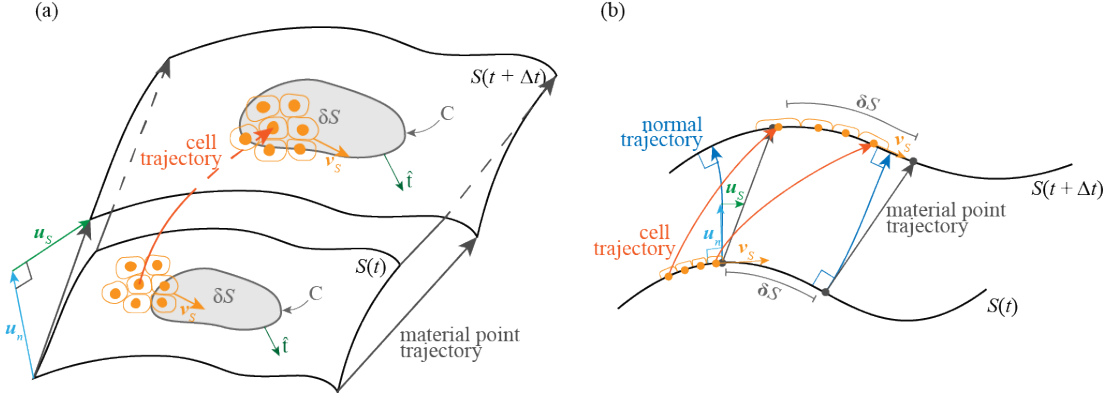


Figure 2.3: (a) Schematic of two dimensional surface portion being considered. The curve C surrounding δS is illustrated as well as its outward facing normal \hat{t} . (b) One dimensional schematic of portion of interface being examined. The normal and tangential components of the surface velocity are annotated in blue and green respectively. Illustrative cells are included in orange, with the tangential flux of cells into δS annotated in orange. The grey arrows indicate the material trajectories of the surface. Cell trajectories and normal trajectories are also annotated.

defined as

$$\left(\frac{\partial \rho}{\partial t} \right)_m = \frac{d}{dt} \rho(\mathbf{r}_S(t), t).$$

The material derivative obeys standard rules of differentiation, so that differentiating Equation (2.2) gives

$$\left(\frac{\partial \rho}{\partial t} \right)_m = \frac{1}{\delta S} \left(\frac{\partial \delta N}{\partial t} \right)_m - \frac{\rho}{\delta S} \left(\frac{\partial \delta S}{\partial t} \right)_m. \quad (2.3)$$

The first term on the right hand side of Equation (2.3) corresponds to changes in density induced by changes in the number of cells residing in δS . The second term on the right hand side of Equation (2.3) describes changes in cell density due to local changes in the area of the portion of interface δS during its

evolution. In the first term, the number of cells may change due to proliferation, death, or net transport from the surrounding portions of the surface. The change in cell number due to proliferation and elimination can be expressed by $(P - A)\delta N(t)$ where P is the per capita proliferation rate, and A is the per capita cell elimination rate. The cell elimination rate may model cell death (apoptosis), detachment from the surface (for example anoikis), or embedment into the tissue. To describe the influence of tangential motion of the cells on cell density changes at position \mathbf{r}_s , we introduce the tangential flux of cells, $\mathbf{J}(\mathbf{r}_s, t)$. This cell flux is measured with respect to material points of the surface, which are themselves transported in space. It represents the number of cells crossing the boundary C of δS per unit length per unit time (Figure 2.3a). The total number of cells leaving and entering δS is thus calculated by the line integral of the flux of cells along C , where C is the curve surrounding δS , with unit normal given by $\hat{\mathbf{t}}$ (Figure 2.3a). Therefore, the total rate of change of cell number in δS is

$$\left(\frac{\partial \delta N}{\partial t} \right)_m = - \oint_C \mathbf{J} \cdot \hat{\mathbf{t}} \, dl + (P - A)\delta N(t). \quad (2.4)$$

Since δS is a small element of surface, the line integral in Equation (2.4) can be written in terms of the surface divergence of \mathbf{J} , which can be formally defined as

$$\nabla_S \cdot \mathbf{J} = \frac{1}{\delta S} \oint_C \mathbf{J} \cdot \hat{\mathbf{t}} \, dl, \quad \text{as } \delta S \rightarrow 0 \quad (2.5)$$

(Arnoldus, 2006). Thus, in the limit of an infinitesimally small area of the interface δS , the change in density due to the change in number of cells in δS in Equation (2.3) is given by

$$\frac{1}{\delta S} \left(\frac{\partial \delta N}{\partial t} \right)_m = -\nabla_S \cdot \mathbf{J} + (P - A)\rho. \quad (2.6)$$

Equation (2.6) represents the fact that the surface divergence of the flux on a curved manifold is related to local changes in surface density (Arnoldus, 2006), much like, in the Euclidean space, the divergence of the flux is related to local changes in volumetric density.

To evaluate the second term of on the right hand side of Equation (2.3), we examine the rate at which δS changes following the material trajectories of $S(t)$. This depends on the local mean curvature,

$$\kappa = \nabla_S \cdot \mathbf{n}, \quad (2.7)$$

and is given by

$$\left(\frac{\partial(\delta S)}{\partial t} \right)_m = \delta S (u_n \kappa + \nabla_S \cdot \mathbf{u}_S). \quad (2.8)$$

where \mathbf{u}_S is the tangential component of the surface velocity and \mathbf{u} (Figure 2.3). Equation (2.8) is derived using the equation for the change of a material area element over time from Batchelor (1976), see 2.A for details. In our notation, κ is defined such that $\kappa < 0$ indicates concavity and $\kappa > 0$ indicates convexity.

Substituting Equations (2.6) and (2.8) into Equation (2.3), we find that the evolution of the surface density of cells following material trajectories of the interface is governed by

$$\left(\frac{\partial \rho}{\partial t} \right)_m = -\nabla_S \cdot \mathbf{J} - \rho u_n \kappa - \rho \nabla_S \cdot \mathbf{u}_S + (P - A)\rho. \quad (2.9)$$

If cell migration includes advection and diffusion, the tangential flux of cells can be written as

$$\mathbf{J} = \rho \mathbf{v}_S - D \nabla_S \rho, \quad (2.10)$$

where \mathbf{v}_S is the tangential velocity of the cells with respect to the surface and $-D \nabla_S \rho$ corresponds to lateral diffusive flux along the curved interface where ∇_S is the surface gradient of ρ , that is the derivative of ρ on the manifold $S(t)$ (Pressley, 2010). In this case, the evolution of the surface density of cells, Equation (2.9) becomes

$$\begin{aligned} \left(\frac{\partial \rho}{\partial t} \right)_m &= D \nabla_S^2 \rho - \nabla_S \cdot (\rho \mathbf{v}_S) - \rho \nabla_S \cdot \mathbf{u}_S \\ &\quad - \rho u_n \kappa + (P - A) \rho. \end{aligned} \quad (2.11)$$

It is possible to determine the rate of change of cell density following other trajectories than the material points of the interface. The evolution equation for cell density takes a particularly convenient form when expressed following trajectories normal to the interface at each time (Figure 2.3). We can relate the derivatives of ρ along the normal and material trajectories by

$$\left(\frac{\partial \rho}{\partial t} \right)_n = \left(\frac{\partial \rho}{\partial t} \right)_m - \mathbf{u}_s \cdot \nabla_S \rho \quad (2.12)$$

where $(\partial/\partial t)_n$ represents the time derivative along the normal trajectories, that is trajectories perpendicular to the surface at all times (Wong et al., 1996).

Substituting Equation (2.11) into Equation (2.12) gives

$$\begin{aligned} \left(\frac{\partial \rho}{\partial t} \right)_n &= D \nabla_S^2 \rho - \nabla_S \cdot (\rho(\mathbf{v}_S + \mathbf{u}_S)) \\ &\quad - \rho u_n \kappa + (P - A) \rho. \end{aligned} \quad (2.13)$$

The first term on the right hand side of Equation (2.13) is the Laplace-Beltrami operator applied to the surface density of cells and describes the tangential diffusion of cells along the curved tissue surface (Berger, 2002). The second term describes the influence of tangential velocities of the cells \mathbf{v}_S and of the tissue surface \mathbf{u}_S , respectively. The fourth term encapsulates the collective cell crowding or spreading effect of curvature, and the last term describes the gain or loss of cells from the group of tissue-synthesising cells. Equations (2.11) and (2.13) are general conservation equations for cells moving by advection and diffusion with respect to a surface which is itself moving and deforming. In 2.B, we show that these equations are a generalisation of similar conservation equations of surface-bound quantities derived in the literature without tangential advection.

The tangential velocities of both the surface and the cells in Equation (2.13) can be chosen to describe multiple biological tissue evolution scenarios. The tangential velocity \mathbf{v}_S can represent for example epithelial cells moving with respect to a basal membrane which may itself be transported in space with velocity \mathbf{u} . Biological situations where cells are not physically transported by a moving tissue interface may be modelled by assuming that there is no tangential movement of the interface ($\mathbf{u}_S = 0$) while cells may still have tangential velocity ($\mathbf{v}_S \neq 0$). This can occur in the case of bone resorption for example, where material points of the bone interface do not move laterally but osteoclasts living on the interface may (Lassen et al., 2017). It is important to note that although the velocity of the tissue surface and the cells may not be distinguishable for modelling the evolution of the tissue interface and changes in cell density, the distinction between these velocities can be important for modelling the tissue material properties produced (Figure 2.2b, Buenzli (2016)), as we will illustrate in our application of the model to bone formation.

In our applications, for simplicity in the numerical solution, we will look at two dimensional problems where the interface is described by a one-dimensional tissue interface, that is, a curve in two-dimensional space. In these situations, Equation (2.13), can be written as

$$\left(\frac{\partial \rho}{\partial t} \right)_n = D \frac{\partial^2}{\partial l^2} \rho - \rho u_n \kappa - \frac{\partial}{\partial l} (\rho(v_S + u_S)). \quad (2.14)$$

where $\partial/\partial l$ is the derivative with respect to the arc length of the surface, which is the one dimensional equivalent of the surface divergence and surface gradient (Redžić, 2001). In the applications presented in Section 3, we solve the coupled equations (2.1) and (2.14), where the tangential cell velocity is given various forms and the ensuing behaviour is analysed.

2.1 Numerical method

Solving Equations (2.1) and (2.14) requires solving a PDE on a moving boundary where the boundary motion is coupled with the PDE solution. To achieve this, we use an efficient hybrid computational method, the cell-based particle method (CBPM), developed in Leung and Zhao (2009); Leung et al. (2011) and Hon et al. (2014). In this method, the interface is represented by Lagrangian marker particles which are each associated with a grid cell of an underlying Eulerian grid with grid cell length Δx . The grid is used to redistribute the particles along the moving interface to maintain quasi-uniform sampling. Furthermore, scalar quantities, such as cell density, can be associated directly with the marker particles (Leung and Zhao, 2009). This is an advantage over level-set like methods, which require additional scalar fields similar to the level-set function to represent surface-bound quantities (Alias and Buenzli, 2019). The interface is evolved over discretised timesteps Δt by advecting the marker par-

ticles according to a velocity field. Local quadratic least squares interpolation of the interface and of the surface density of cells is then used to estimate the interface curvature and to evaluate spatial derivatives. The reader is referred to the Supplementary Information, Leung and Zhao (2009); Leung et al. (2011); Hon et al. (2014), and Hegarty-Cremer (2020) for more details.

3 Results

We now apply our mathematical model to cases of tissue growth where the inclusion of tangential cell advection allows us to model new biologically relevant situations. First, we validate the numerical method by solving simplified equations which test the two migration mechanisms of Equation (2.14), that is tangential cell advection and diffusion, as well as the crowding and spreading effect of curvature. These solutions are compared with analytic solutions. Then we model bone pore infilling and explore the generation of different orientations of collagen fibrils in infilled osteons, as illustrated in Figure 2.1b. Finally, we model bone resorption, where osteoclasts tunnel through old bone tissue and investigate the influence of tangential cell velocity for the stability of travelling-wave-like resorption fronts observed during the resorption of cortical bone.

3.1 Validation of the numerical method

To validate our implementation of the CBPM for solving Equation (2.14), we compare numerical simulations to analytical solutions in a simple setting where density is decoupled from the normal speed of the interface, that is we replace Equation (2.1) with $u_n = c$, where c is a constant. We also set $D = 0$ and choose a circular initial interface with initial radius R_0 . In this case, the interface remains a circle at all times and it expands in the normal direction with radius $R(t)$. We parameterise the circle using the arc length l and solve for ρ on the

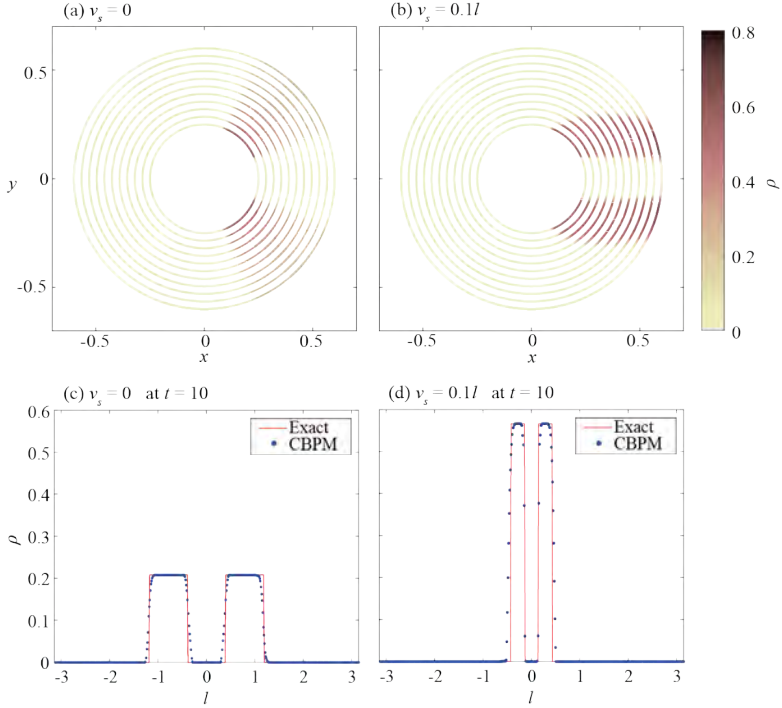


Figure 2.4: Expanding circle with $u_n = 0.035$ and with or without tangential velocity: comparison between CBPM simulations and exact solutions. (a) and (b) Solution obtained using CBPM with $v_s = 0$ and $v_s = 0.1l$, respectively, with interface shown at regular time intervals ($\Delta T = 1$). (c) and (d) Exact and CBPM solution density representation over arc length parameter at $t = 10$ with $v_s = 0$ and $v_s = 0.1l$, respectively. The discretisation used is $\Delta x = 0.01$ and $\Delta t = 0.01$.

domain $-\pi < l < \pi$. The governing equations become

$$\frac{dR}{dt} = c \quad (2.15)$$

$$\frac{\partial \rho}{\partial t} + v_s \frac{\partial \rho}{\partial l} = \frac{\partial v_s}{\partial l} \rho - \rho c \kappa. \quad (2.16)$$

We assume an arbitrary initial cell density distribution $\rho(l, 0) = \rho_0(l)$ and an initial radius $R(0) = R_0$, and impose periodic boundary conditions $\rho(-\pi, t) =$

$\rho(\pi, t)$. The solution for $R(t)$ is

$$R(t) = ct + R_0, \quad (2.17)$$

so that $\kappa(t) = 1/(ct + R_0)$. To test the advection term in Equation (2.14), we assume that cells are subject to the tangential cell velocity field $v_S = -al$ where a is constant. The governing equation for ρ becomes a quasilinear advection equation, which can be solved using the method of characteristics (Evans, 2010), giving

$$\rho(l, t) = \frac{\rho_0(l e^{at}) R_0 e^{at}}{ct + R_0}. \quad (2.18)$$

We test numerically both dilution of cells without advection, $a = 0$, and dilution of cells with advection, $a \neq 0$. Figure 2.4 compares this analytical solution to the numerical solution obtained using the CBPM. In Figure 2.4, the initial condition for density is piecewise constant such that $\rho = 0.5$ when $\pi/8 < |l| < 3\pi/8$ and $\rho = 0$ elsewhere. There is excellent alignment between the analytic solution in Equation (2.18) and the one obtained by the CBPM both with and without tangential velocity. The small discrepancies are due to some degree of smoothing of the numerical solution, which originates from the local interpolation step of the CBPM. As expected, if the numerical discretisation is refined, the match improves (data not shown).

To validate our implementation of the CBPM for problems that include diffusive transport, we solve the diffusion equation on a stationary circle using the CBPM. With a sinusoidal initial condition $\rho_0(l) = 0.5 + 0.5 \sin(l)$ and periodic boundary conditions the analytic solution is given by

$$\rho(l, t) = 0.5 + 0.5 \sin(l) e^{-4Dt}. \quad (2.19)$$

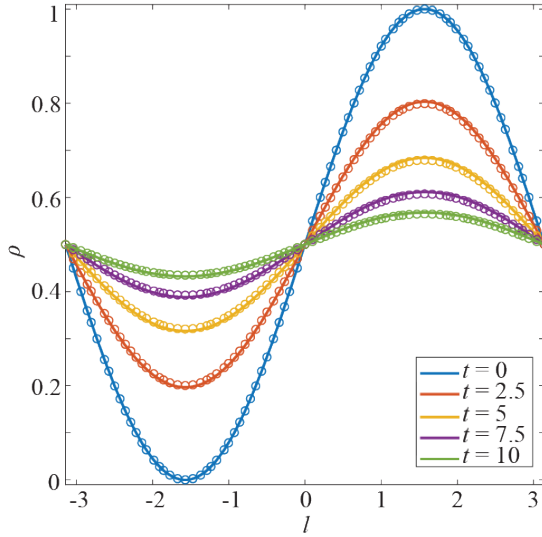


Figure 2.5: Analytic (solid line) and CBPM (points) solutions for diffusion around a stationary circle. The discretisation used is $\Delta x = 0.01$ and $\Delta t = 0.01$.

The results of the CBPM are compared with this solution at different times in Figure 2.5. Again, there is an excellent agreement between the solutions.

3.2 Circular bone pore infilling

We now consider the case of a circular bone pore being infilled by a population of osteoblasts distributed uniformly along the pore's perimeter. This can be thought of as the infilling of a cortical bone osteon seen in a transverse cross section. New bone tissue is gradually produced such that the initial interface is moving inwards while retaining a circular shape. As infilling proceeds, the density increases as a result of the systematic effect of curvature (Buenzli, 2014, 2016). We examine three cases of tangential cell velocity: no tangential velocity, constant tangential cell velocity, and time-dependent tangential cell velocity such that cells reverse their motion with respect to the interface at specific times (Figure 2.6). By rotation symmetry, in these simulations, the density remains uniform at all times, but it is time dependent due to the shrinkage of the bone

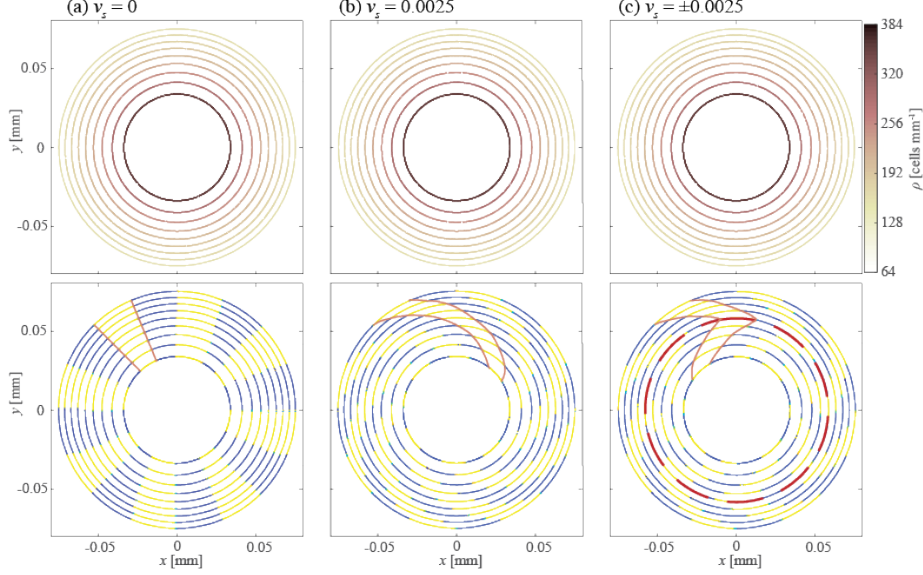


Figure 2.6: Circular pore infilling results with cell secretion rate $k = 7.8125e-06$ mm/day and with varying tangential cell velocity. In each figure the initial interface is the outermost ring and the interface is shown at regular time intervals ($\Delta T = 3$ days). The top figures show density and interface position while the bottom figures show cell trajectory tracking and interface position with a single cell trajectory annotated in orange. (a) Infilling circle without tangential velocity. (b) Infilling circle with tangential velocity $v_s = 0.0025$ mm/day. (c) Infilling circle with tangential velocity $v_s = 0.0025$ mm/day when $t < 12.5$ days and $v_s = -0.0025$ mm/day when $t \geq 12.5$ days. The location of the change of direction is emphasised in a red dashed circle. The discretisation used is $\Delta x = 0.001$ mm, $\Delta t = 0.075$ days.

surface area as infilling proceeds.

The evolution of density and interface position is the same across the three cases (Figures 2.6a–c). However, the cell trajectories in space are distinct, and this creates different tissue material properties (Figures 2.6d–f). To visualise cell trajectories in Figures 2.6d–f, cells are stained either in blue or in yellow. This is achieved in the CBPM by assigning a new scalar property to each marker particle, which is simply advected along the cell trajectories. In Figure 2.6d, cells have no tangential motion hence their trajectories are moving along straight

radial lines. However, in Figures 2.6e and 2.6f, the cells move tangentially to the surface, thus their trajectories spiral inwards. The results in Figure 2.6f illustrate how one may explain a change in anisotropic tissue material properties. As collagen fibrils secreted by osteoblasts may be weaved according to the directionality induced by cell migration, the change in cell trajectory orientation could be used to describe the change in collagen fibre orientation in lamellar bone and the consequent plywood structure (as illustrated in Figure 2.1b).

3.3 Bone resorption in basic multicellular units

We now examine the resorption phase of a bone remodelling event as another example where the tangential velocity of cells may be important for the evolution of the tissue interface. In bone resorption, bone tissue is removed by osteoclasts attached to the bone surface. The resorption of bone matrix by osteoclasts creates a cavity which maintains consistent cellular organisation and shape at the resorption front (Figure 2.1c) (Jaworski and Hooper, 1980; Ryser et al., 2009; Buerli, 2010, 2011, 2014; Buerli et al., 2012; Lassen et al., 2017). We apply our tissue growth model to this situation to show that to maintain this stable travelling resorption front, directed tangential osteoclast motion is required (Figure 2.1c).

Recent works have suggested that osteoclasts at the front of basic multicellular units may remain at this position for a long period of time (Lassen et al., 2017), unlike previous suggestions that osteoclasts move down the cavity walls (Burger et al., 2003; Buerli et al., 2012). We show here, based on simple numerical simulations, that a stable resorption front requires cell guidance mechanisms to steer osteoclasts back toward the tip of the cavity (Figure 2.1c). Without such directed motion, the cavity rapidly expands out and osteoclasts

move away from each other (Figure 2.7a). Figures 2.7b and 2.7c show numerical simulations where two different types of signals are used to steer osteoclasts back toward the tip of the cavity. The first signal modelled can be thought of as haptotaxis, which is a cell guidance mechanism in response to adhesion gradient on the substrate generated by cell binding to substrate molecules (Davies, 2013). The second is chemotaxis, which describes cell guidance through a chemical gradient (Murray, 2002). Other signals could also be considered, such as mechanical signals. Mechanical loading could be modelled by including a strain field as presented in Smit and Burger (2000). This could be implemented either as an external signal, where the mechanical strain could be transduced into molecular signals by osteocytes, or an internal signal, where osteoclasts could directly sense the strain.

Osteoclasts work in close contact with other cells lining the cavity walls, called reversal cells, which may provide haptotactic signals such as receptor activator of nuclear factor kappa-B ligand (RANKL) (Martin et al., 2004; Lassen et al., 2017). Here we assume the haptotactic signal induces a tangential velocity to the osteoclasts, $v_s = a l$, where l is the arc length measured along the cavity wall from the tip and a is a positive constant. This is similar to Section 3.2 where $l > 0$ on the upper part of the cavity and $l < 0$ on the lower part of the cavity. Using this form of tangential cell velocity, it can be seen from Figure 2.7b, that a stable resorption front is formed. Between $t = 0$ and approximately $t = 3$ days, there is a transient period, where the shape of the resorption front evolves until a balance between the advection-induced crowding and curvature-induced spreading of the osteoclasts is achieved. After this transient, the cell density profile and the cavity front shape is maintained as it progresses through the bone tissue.

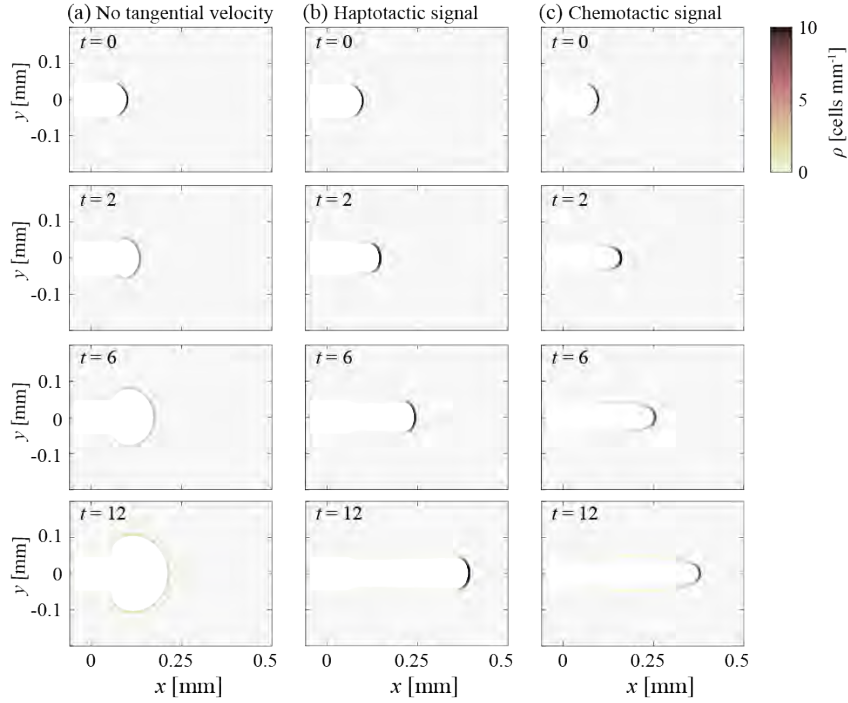


Figure 2.7: Bone resorption results with different forms of tangential cell advection. The time is shown in days and the spatial unit is mm. The resorption rate is 0.025 mm/day ($k = -0.025$). (a) Resorption front behaviour with no tangential velocity pulling cells. (b) Haptotactic signal: arc length dependent tangential velocity. The proportionality constant between the arc length distance and the tangential velocity is $a = 0.6$. (c) Chemotactic signal: tangential velocity determined by the projection of an external gradient field on the interface. The discretisation used is $\Delta x = 0.00375$, $\Delta t = 0.02$.

Alternatively, we model chemotaxis by projecting a velocity gradient field, such as one created by a gradient of chemical concentration $-b\nabla C$, onto the cavity surface and taking this projection as the tangential velocity,

$$v_S = -b\nabla C \cdot \boldsymbol{\tau}. \quad (2.20)$$

Indeed, active osteoclasts remain bound to the interface, therefore they can only

explore the tangential component of the chemical gradient field. This gradient could be due to signalling molecules derived from mechanically-stimulated osteocytes embedded in bone matrix, that steer osteoclasts toward specific areas of bone needing repair (Turner et al., 1994; Marotti, 2000; Ryser et al., 2009; Lerebours et al., 2016), such as high mobility group box protein 1 (HMGB1) (Yang et al., 2008) and colony-stimulating factor 1 (CSF-1) (Harris et al., 2012), or it may be due to other chemotactic molecules from the bone microenvironment, such as monocyte chemoattractant protein-1 (MCP-1/CCL2) (Wu et al., 2013), and the chemorepulsing sphingosine-1-phosphate (S1P) (Ishii et al., 2010). For the results presented here, we simply take $-b\nabla C = [0, -2.5 \operatorname{sgn}(y)y^2]$, which is a velocity field in the y direction with streamlines pointing towards the centerline of the cavity. Figure 2.7c shows that, similarly to the haptotaxis results, stable resorption front behaviour is obtained after an adjustment period between $t = 0$ and $t = 3$ days.

Both forms of cell guidance signal result in stable resorption fronts, but they lead to different resorption cavity shapes, indicating that the type of signal is also important for the resorption front. The chemotactic signal results in a wider distribution of osteoclasts around the resorption front compared to the haptotactic signal, which results in a high concentration of cells on a narrow portion of the interface. Due to coupling, these differences in cell densities are reflected in the shape of the resorption fronts. However, the speed of these resorption fronts is comparable, with the haptotactic signal canal reaching $x \approx 0.345$ mm at $t = 12$ days and the chemotactic signal canal reaching $x \approx 0.34$ mm at $t = 12$ days. These speeds align well with expected speeds of resorption cavities (30-40 $\mu\text{m}/\text{day}$) (Jaworski et al., 1981; Lassen et al., 2017).

Furthermore, the diameter of the canals falls within the values stated in Lassen et al. (2017) BMU analysis. The ‘Level 1’ canal diameters (25 μm from the front) are 58.8 μm for the chemotaxis and 87.7 μm for the haptotaxis, and the ‘Level 2’ canal diameters (325 μm from the front) are both around 100 μm . The range of diameters found in Lassen et al. (2017) for Level 1 is \approx 30-180 μm with the mean being 80 μm and for Level 2 it is \approx 110-390 μm with the mean being 200 μm .

4 Discussion and conclusion

Tangential cell motion generated by cell guidance mechanisms is important in several situations of tissue growth, such as growth occurring at an angle with respect to the tissue surface, and the generation of anisotropic tissue properties. We have developed a new mathematical model for tissue growth under collective curvature control to incorporate such directed cell guidance mechanisms by including tangential cell motion. The model is derived from conservation principles applied to the surface density of tissue-synthesising cells. This derivation results in a PDE for cell density on a moving boundary, which is coupled with the boundary motion. The governing equations are expressed in covariant form, that is, they are independent of a choice of surface parameterisation and coordinate system. We solve the model numerically using a hybrid front-tracking computational method, the CBPM, and find good agreement with analytic solutions.

Experimentally, the interaction between curvature control of tissue growth and directed cell motion is difficult to investigate, due to the challenge of controlling evolving tissue geometries. Crowding and spreading effects on rates of tissue progression are a consequence of space constraints that may be masked by cell behavioural influences in experiments. The development of mathematical mod-

els that account for such collective effects can help disentangle geometric and cell behavioural influences of tissue growth (Cai et al., 2007; Alias and Buenzli, 2018; Buenzli et al., 2020). The example of bone tissue resorption developed in this paper (Figure 2.7) illustrates the importance of taking into consideration both the mechanistic influence of curvature on osteoclast density, and the tangential motion of osteoclasts with respect to the bone interface. Without accounting for the mechanistic influence of curvature, the presence of a driving force steering osteoclasts toward the centerline of the resorption cavity would not be highlighted. Without tangential motion of osteoclasts at the tip of bone resorption cavities, our results suggest that stable cavity shapes are not possible.

Our mathematical model describes the joint evolution of the tissue interface and tissue-synthesising cell density. The example of bone pore infilling in Figure 2.6 illustrates that directed motion of cells can generate anisotropies in tissue material properties. While we did not model tissue generation explicitly, our model may be coupled with more detailed tissue generation mechanisms that include creation and destruction of tissue material at moving interfaces, as well as tissue maturation mechanisms, based on bulk and surface mass balance (Cumming et al., 2010; Buenzli, 2015, 2016). Our model thus provides a basis for further explorations into the relationship between the spatial organisation of anisotropic tissue material properties, and the dynamics of their creation. Biological experimental data often takes the form of tissue samples or biopsies representing single snapshots in time of the state of the tissue. This type of data contains detailed spatial information about the organisation of a tissue, but it does not offer a detailed picture of its time evolution. The provision of mathematical links between features recorded in the state of a tissue and the dynamics of its formation may allow us to deduce how a tissue has been produced given an analysis

of its material properties. In bone tissues, for example, several features of bone formation are recorded, such as osteocyte density (Buenzli, 2015), mineral density (Buenzli, 2016; Lerebours et al., 2020), and tetracycline labels and lamellae, which provide information about past location of the bone interface (Martin et al., 2004; Buenzli, 2014; Andreasen et al., 2018). This type of information is used in bioarcheology to estimate archaeological age and activity (Buckberry and Chamberlain, 2002; Maggiano et al., 2008; Mays, 2010). An analysis of lamellae patterns in bone cross sections could provide more information about osteoblast behaviour, and provide more insights in cases of irregular bone formation patterns such as drifting osteons (Robling and Stout, 1999; Maggiano, 2012) and bone disorders.

Discretising PDEs on moving boundaries is a challenging problem of applied mathematics. In this paper, we restricted our model to two dimensional applications for simplicity. Clearly, applications of our model to three-dimensional tissue growth are of interest (Figure 2.1) (Guyot et al., 2014; Goriely, 2017; Ambrosi et al., 2019; Ehrig et al., 2019). Sophisticated techniques have been developed to simulate the evolution of interfaces in three-dimensional complex systems (Sethian, 1999; Tryggvason et al., 2001; Glimm et al., 2001; Shin and Juric, 2002; Osher and Fedkiw, 2003; Du et al., 2006; Leung and Zhao, 2009; Hon et al., 2014). While the level-set-like method developed in (Alias and Buenzli, 2019) for curvature-controlled tissue growth may be suitably adapted to include tangential cell velocity, the CBPM of Hon et al. (2014) used in this work is also applicable to three-dimensional interfaces.

Acknowledgements

This work is supported by the Australian Research Council (DP180101797, DP200100177), the Centre for Biomedical Technologies, Queensland University of Technology (QUT), and the Institute of Health and Biomedical Innovation (IHBI), QUT, as well as the VELUX foundation (Project no. 25723).

Appendices

2.A Evolution of local surface area

We start with the equation for the rate of change of a vector area element ($\delta\mathbf{S} = \mathbf{n}\delta S$) of a material surface from [Batchelor \(1976\)](#),

$$\left(\frac{\partial(\delta\mathbf{S})}{\partial t} \right)_{\mathbf{m}} = \delta\mathbf{S}(\nabla \cdot \mathbf{u}) - (\nabla \mathbf{u})^T \delta\mathbf{S}, \quad (2.21)$$

where $\nabla \mathbf{u}$ is the Jacobian matrix of \mathbf{u} . Following [Stone \(1990\)](#), we take the inner product with \mathbf{n} , to obtain an expression for the change in local surface area, δS , over time,

$$\left(\frac{\partial(\delta S)}{\partial t} \right)_{\mathbf{m}} = \delta S [\nabla \cdot \mathbf{u} - \mathbf{n}^T (\nabla \mathbf{u}) \mathbf{n}]. \quad (2.22)$$

The right hand side of Equation (2.22) corresponds to subtracting to the total divergence of \mathbf{u} , that is, to the trace of the Jacobian matrix of \mathbf{u} , the normal component of the trace, $\mathbf{n}^T (\nabla \mathbf{u}) \mathbf{n}$. This gives the surface divergence operator of \mathbf{u} , so that

$$\left(\frac{\partial(\delta S)}{\partial t} \right)_{\mathbf{m}} = \delta S \nabla_S \cdot \mathbf{u} \quad (2.23)$$

Decomposing \mathbf{u} into its tangential and normal components, $\mathbf{u} = u_n \mathbf{n} + \mathbf{u}_S$, one gets

$$\begin{aligned} \left(\frac{\partial(\delta S)}{\partial t} \right)_{\mathbf{m}} &= \delta S (\nabla_S \cdot (u_n \mathbf{n}) + \nabla_S \cdot \mathbf{u}_S) \\ &= \delta S (u_n \kappa + \nabla_S \cdot \mathbf{u}_S) \end{aligned} \quad (2.24)$$

where the second equality in Eq (2.24) uses the fact that the surface divergence of the unit normal vector is the mean curvature of the surface, $\kappa = \nabla_S \cdot \mathbf{n}$ (Goldman, 2005), and that the surface gradient is perpendicular to \mathbf{n} , so that $\mathbf{n} \cdot \nabla_S u_n = 0$.

2.B Comparison with the literature

In multiphase physico-chemical systems, similar evolution equations to Equation (2.11) are derived for the surface transport of surfactants at the interface between two phases (Stone, 1990; Wong et al., 1996; Xu and Zhao, 2003). A difference between such physical systems and the biological systems we are modelling is the coupling between the surface velocities and the cell density via Equation (2.1). Cell density affects interface evolution, whereas in multiphase physico-chemical systems, surface evolution is usually assumed to be independent of surfactant density. Furthermore physico-chemical system models do not consider the tangential velocity of a surfactant with respect to the surface.

In Stone (1990), surfactant mass balance equations are derived, however the nature of the time derivative of surfactant density is unclear (Wong et al., 1996). Time derivatives in Stone (1990) implicitly represent changes following paths normal to the interface. The surfactant mass balance results obtained in Wong et al. (1996) make the nature of the time derivative explicit by being derived using an explicit parameterisation of the interface. The parameterisation is general in the sense that the coordinate system is not necessarily bound to the material points of the interface. If we set $\mathbf{v}_S = 0$, $A = P = 0$ in Equation (2.13), we fall back on Equation (7) from Stone (1990) following normal trajectories, and Equation (5b) from Wong et al. (1996) equation if the timelines of their parameterisation are taken to be following the normal trajectories of the surface.

Neither the equations in Wong et al. (1996) nor Stone (1990) include coupling between the interface speed and density of cells nor tangential velocity. The derivation in Alias and Buenzli (2017) includes coupling between cell density and interface speed, but the cells have no tangential advection, that is, their only lateral motion is diffusive. To compare our model with that in Alias and Buenzli (2017), the cell velocities in Equation (2.13) must be chosen such that the cells move along the normal trajectories of the interface. Therefore, if we set $v_S = -u_S$, the governing equations agree.

2.C Numerical Discretisation

We provide more detail on the numerical method used to solve our mathematical model, the cell-based particle method (CBPM). As well as the advantages of the CBPM discussed in the main text, the CBPM also allows for efficient detection and implementation of topological changes during fusion or fragmentation of the interface without requiring information about the connectivity of the marker particles. This method is of $\mathcal{O}(N)$ in computational load, where N is the number of marker particles. This is to be contrasted with standard level set methods on $N \times N$ grids, which have $\mathcal{O}(N^2)$ computational load, or $\mathcal{O}(N \log N)$ for local level set methods (Sethian, 1999). The CBPM method for solving PDEs on moving boundaries gives approximately conservative solutions (Leung and Zhao, 2009).

The CBPM algorithm is comprised of four main steps: initialisation, movement, resampling, and activation or deactivation. The initialisation stage declares the set of active marker particles which are used to track the interface, its geometry, and any associated scalar quantities. Initialisation requires an explicit param-

terisation of the initial surface, $\gamma(m)$, where m is a parameterisation variable for the one-dimensional surface γ in two dimensional space. The movement stage requires a velocity field which is used to advect the marker particles, and thus to evolve to position of the interface. This velocity field can be space and time dependent, and may be determined by external processes, or be coupled with the evolution of intrinsic properties of the system. In our case, it is intrinsic and implicitly time dependent since it depends on the surface density of cells. To solve the partial different equation (PDE) for a scalar quantity residing on the moving interface, each marker particle is supplemented with a scalar value, which is evolved according to the particular PDE after the motion step of the marker particles.

The resampling stage assures a quasi-uniform sampling of the interface through local interpolation. The local interpolation of the interface is expressed in a local coordinate system aligned with the local surface unit normal and calculated using quadratic least squares. The interpolation is used to update the unit normals, curvature, and any other local surface properties of interest, as well as to resample the active marker particles and calculate spatial derivatives in Equation (13). Finally, the activation and deactivation stage deactivates marker particles associated with underlying grid cells which no longer contain part of the interface, and activates marker particles associated with underlying grid cells into which a portion of the interface has now moved. The activation and deactivation stage also detects changes due to topological changes of the interface including collision, fusion, or fragmentation. For more details on the algorithm see to [Leung and Zhao \(2009\)](#); [Leung et al. \(2011\)](#), and [Hon et al. \(2014\)](#). Below we describe how the method is applied to our problem.

To solve Equations (1) and (13), we first need to choose an advective velocity field in the two dimensional space. Several choices are possible, including paths normal to the interface at all times, material points of the interface, and cell trajectories. Since cells may carry intrinsic information and it is expected that the numerical resolution of cell density changes will be more accurate along these trajectories, we choose to move the marker particles along cell trajectories. We thus define the intrinsic velocity field that governs the evolution of the surface by

$$\mathbf{V}_\gamma = u_n \mathbf{n} + v_S \boldsymbol{\tau}, \quad (2.25)$$

and we use a forward Euler scheme to evolve the positions of the marker particles in time for simplicity. More advanced time stepping schemes can be devised (Leung and Zhao, 2009; Leung et al., 2011; Hon et al., 2014), but in practice, moving boundary problems are more sensitive to spatial discretisation accuracy than time discretisation accuracy (Osher and Fedkiw, 2003). Equation (13) is solved after interface motion using operator splitting with forward Euler, with the first step solving for curvature control,

$$\rho_t^* = \rho_{t-1} + \Delta t(\rho \kappa u_n), \quad (2.26)$$

where the * indicates an intermediary step in the solution for ρ_t and Δt is the time step. Given there is a local interpolation for both the surface and the density values, denoted by

$$\hat{\gamma}(m) = \alpha_1 + \alpha_2 m + \alpha_3 m^2, \quad \text{and} \quad (2.27)$$

$$\hat{\rho}(m) = \beta_1 + \beta_2 m + \beta_3 m^2, \quad (2.28)$$

respectively, we can then calculate the diffusion term of Equation (13) by calculating the Laplace Beltrami operator

$$\frac{\partial^2 \hat{\rho}}{\partial l^2} = \frac{1}{g^2} \frac{\partial^2 \hat{\rho}}{\partial m^2} - \frac{1}{g^3} \boldsymbol{\tau} \cdot \frac{\partial^2 \hat{\gamma}}{\partial m^2} \frac{\partial \hat{\rho}}{\partial m} \quad (2.29)$$

directly from the second order interpolation, $\hat{\rho}(m)$. In Equation (2.29), g is the surface metric, $|\partial \hat{\gamma} / \partial m|$. Similarly to the Laplace-Beltrami operator, the final term of Equation (13) can be calculated using the local interpolation. The derivative of v_S with respect to l can be calculated either explicitly or via interpolation depending on the form of v_S . The forward Euler method is then used to step the diffusion and advection operators forward in time,

$$\begin{aligned} \rho_t = \rho_t^* + \Delta t & \left(D \left(\frac{2b_3}{g^2} - \frac{2a_3}{g^4} (a_2 + 2a_3m)(b_2 + 2b_3m) \right) + \right. \\ & \left. - \frac{v_s}{g} (b_2 + 2b_3m) - \rho_t^* \frac{\partial v_S}{\partial l} \right). \end{aligned} \quad (2.30)$$

This concludes the calculation of ρ between timesteps. We also include convergence graphs where we examine the error of the final time solution compared to the analytic solutions presented in Figures 2.4 and 2.5. The error is calculated by comparing the densities at $t = 10$ along the arc length of the surface. For each discretisation, the absolute error is calculated for every marker particle, then the average of these absolute errors is found. The figures show that indeed the error is reducing as the discretisation is refined, and the spatial discretisations chosen for the results presented above are justified.

2.D Effect of resorption constants

Here we present results which show the sensitivity of the resorption behaviour discussed in Section 3.3 to the strength of the cell signals. We present results

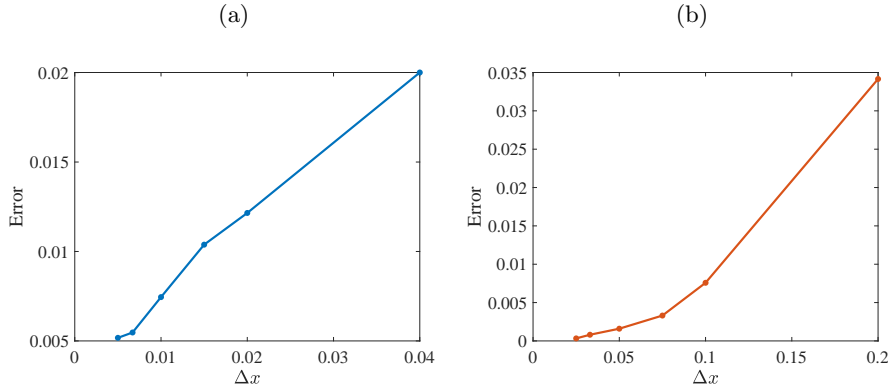


Figure 2.8: Discretisation convergence graphs. (a) Comparison of average absolute error of the advection-only problem (Equation 2.18). The time step is changed with the spatial step, maintaining the relation $\Delta t = \Delta x$. (b) Comparison of average absolute error of the diffusion-only problem (Equation 2.19). The time step is changed with the spatial step, maintaining the relation $\Delta t = \Delta x^2/D$.

for different values of a , the proportionality constant of the haptotactic signal, and different values of b , the proportionality constant of the chemotactic signal.

We also present the result if both signals are linearly combined.

For both signals, we see that increasing the constant of proportionality, and thus increasing the strength of the signal, causes a narrower front which travels faster through the bone (Figure 2.9b and c). Weakening the signal has the opposite effect (Figure 2.9a and c). When combining the two types of signals, we see elements of the behaviours of each. There is a flatter front of the cutting cone, which can be seen in the haptotactic results, but there is also a widening of the channel further back which is characteristic of the chemotactic results. Therefore, through the combination of these two signals, many different resorption behaviours can be modelled.

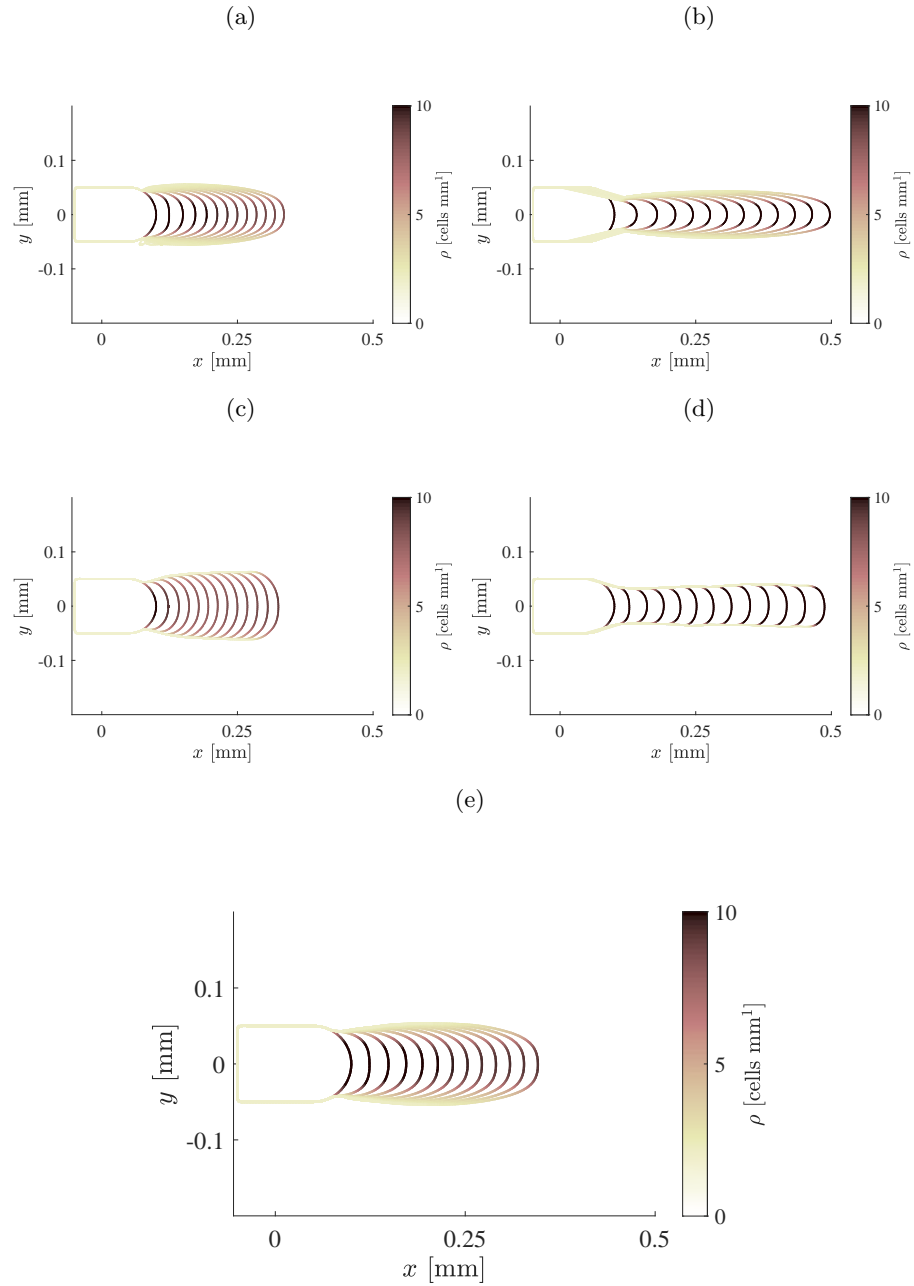


Figure 2.9: Sensitivity analysis of resorption behaviour to proportionality constants. (a) and (b) Chemotactic signals with proportionality constants of $b = 1.25$ and $b = 5$ respectively. (c) and (d) Haptotactic signals with proportionality constants of $a = 0.3$ and $a = 1$ respectively. (e) Combination of chemotactic and haptotactic signals with $b = 1$ and $a = 0.1$.

Chapter 3

Experimental Data Study

1 Introduction

In this Chapter, we consider the application of the mathematical model of curvature control of tissue growth to the infilling of bone pores, called osteons. The mathematical model follows from Polig and Lee (1990); Buenzli (2014) and Alias and Buenzli (2018), and is a specialisation of the mathematical model presented in Chapter 2. The originality of the work presented in this chapter is (i) the development of a systematic, quantitative approach to calibrate the model with experimental data on osteons available through collaboration, and (ii) the examination of hypotheses about different infilling behaviour in atypical osteons.

Osteons are cylindrical structures in dense, load-bearing bone (cortical bone) which are created as a result of the lifelong tissue renewal process in bone, called bone remodelling. Through this process, pores are created by bone-resorbing cells, called osteoclasts, that tunnel through old bone. These pores are subsequently infilled by bone-secreting cells, called osteoblasts (Martin et al., 2004), (Figure 3.1). As infilling progresses, some osteoblasts become embedded into the bone tissue and become a new type of cell, osteocytes (Figure 3.1). Understand-

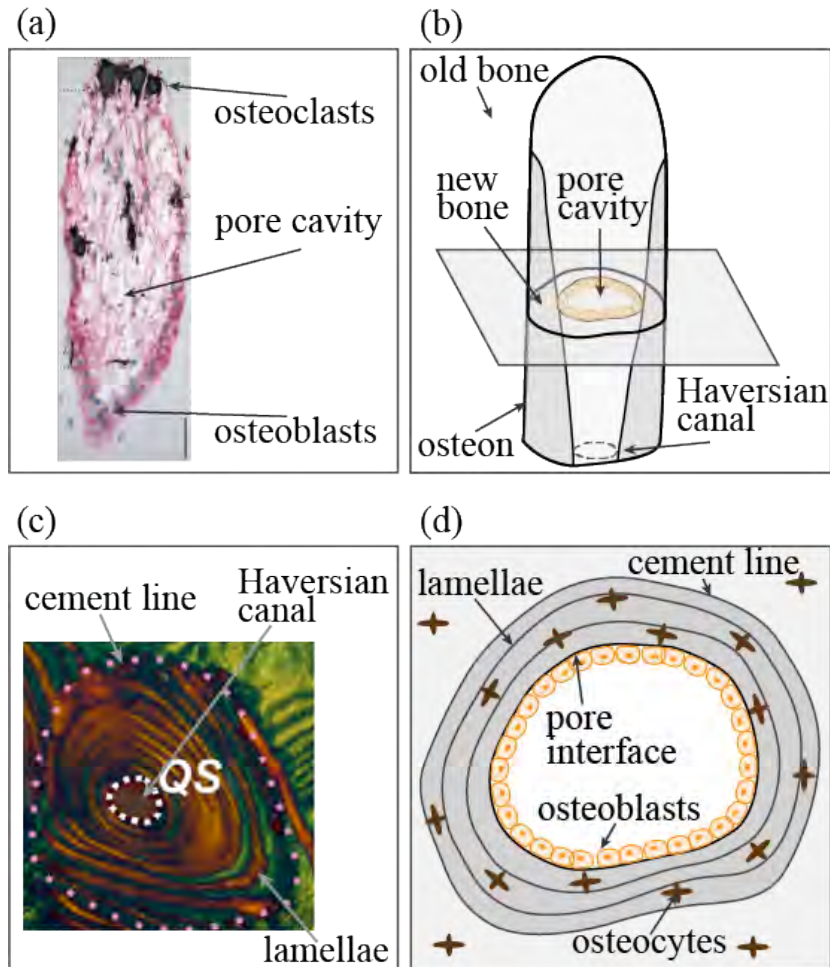


Figure 3.1: Schematics and experimental snapshots of osteon infilling process. Figures (a) and (c) show experimental data of cross sections in the longitudinal and transverse planes respectively, reproduced from Lassen et al. (2017) and Andreasen et al. (2018) respectively. (b) and (d) are diagrams of the process which show characteristics which can be extracted from experimental data

ing the mechanisms that control the infilling of osteons is particularly important as it is known that during age-related bone loss, bone porosity increases as a result of the pores being infilled less with age (Seeman, 2008; Andreasen et al., 2018). However, the effects of the mechanical and geometrical factors that control this process remain poorly understood (Seeman, 2008; Lerebours et al.,

2016). Determining the factors that influence the osteon infilling process *in vivo* presents particular challenges as data cannot be easily extracted while the process is ongoing. Live imaging of bone at this resolution (5-20 μm) cannot be obtained from live human subjects (Perilli et al., 2012). As a result of this, most of the information that is available comes from bone biopsies, i.e. information is only available at single snapshots in time.

By applying our mathematical model to investigate bone-infilling in osteons, our aim is to help disentangle the individual effects of some of the factors of osteon infilling. The data that can be extracted from these samples is the cement line (the initial pore cavity), the Haversian canal (the final pore that remains after infilling has completed), and individual lamellae (bone layers with specific orientations of tissue fibres), which provide records of past locations of the interface (Figure 3.1). Our aim is to provide a more complete picture of the time evolution between the initial pore cavity and the final pore cavity.

2 Experimental Data

The data used to calibrate the tissue growth model to osteon infilling was provided through our collaborators, Thomas Andersen, Christina Andreasen, and Xenia Borggaard (University of Southern Denmark, Odense, Denmark). The data was provided in the form of images of transverse cross-sections of cortical bone taken during forensic examination of human subjects after an unexpected death. None of the subjects showed evidence of pre-existing bone diseases. In this study, we examined eight osteons from males and females aged between 24 and 44 years (Figure 3.2). These samples were chosen because the cement

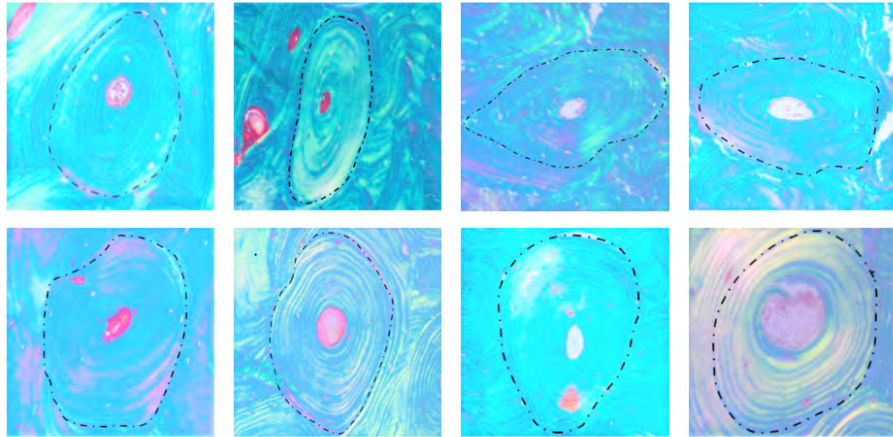


Figure 3.2: Experimental osteon data used. The pink/white elliptical shapes in the center of the cement lines (black dashed lines) are the Haversian canals.

line (outline of initial pore before infilling started) was easy to identify. Our collaborator Xenia Borggaard identified the cement lines using a staining of the osteons, the cement lines are denoted as black dashed lines in Figure 3.2.

The cement line was taken to be the initial condition of the simulation and the outline of the Haversian canal (outline of final pore once infilling has stopped) was used to compare the experimental data and the final state of the simulation.

3 Methods

The mathematical model is the same as described in Chapter 2. In this application, the density of cells in the model is the density of osteoblasts, and the tissue surface is the evolving pore edge during the infilling of the pore with new bone tissue. As this model is applied to relatively regular osteons showing no evidence of tangential interface motion (Figure 3.2), no tangential interface motion is included at this stage ($u_S = 0$), this decision was taken in discussion with

our experimental collaborators. Tangential cell motion is believed to play a role in more atypical osteon structures, such as drifting osteons (see Chapter 4). We note that, although tangential osteoblast motion may be responsible for generating tissue material anisotropies in these osteons (Chapter 2, Section 3.2), this motion does not necessarily influence the evolution of the interface itself, and thus is not considered here ($v_S = 0$). Here, the focus is first to calibrate the model derived in Chapter 2 with the experimental data available, hence we are concerned with the timing and location of intermediate interfaces and not with the generation of anisotropies in the tissue produced.

3.1 Mathematical model

The model is applied in two-dimensions on a transverse cross section of an osteon (Figure 3.1c and d). Limiting the model to two dimensions is reasonable as osteoblasts do not move considerably in the longitudinal (out of the plane) direction (Parfitt, 1994). Without tangential cell velocity, the model is equivalent to the model in Alias and Buenzli (2018). The governing equations of the model are given by

$$u_n = k\rho, \quad (3.1)$$

$$\left(\frac{\partial \rho}{\partial t} \right)_n = D \frac{\partial^2}{\partial l^2} \rho - \rho u_n \kappa - A\rho - Otu_n, \quad (3.2)$$

where $(\partial/\partial t)_n$ indicates the derivative along the normal trajectories of the bone surface (see Equation (2.12)), ρ is the density of tissue-secreting cells (osteoblasts), k is the tissue secretion rate, D is the diffusivity, u_n is the normal speed of the bone surface, κ is the local mean curvature, and the last two terms are sink terms representing the rate at which the pool of active, tissue-secreting osteoblasts is depleted. The sink terms are split into a general term A , and

Otu_n which is the rate at which osteoblasts are embedded into the tissue and become osteocytes (Buenzli, 2015). The three main mechanisms included in this model are:

1. The crowding and spreading of osteoblasts according to curvature;
2. Osteoblasts diffusion along the tissue surface; and
3. The depletion of osteoblasts.

In Alias and Buenzli (2018) different geometric dependencies for the cell-specific tissue secretion rate, k , and the rate at which tissue-secreting cells are lost, A , were examined. In circular pore geometries, experimental evidence suggests that A and k depend on pore radius, R (Marotti et al., 1976; Alias and Buenzli, 2018). However, when pores are not circular, the dependence on R may be interpreted as either curvature, or porosity ϕ . The best combination of functional forms was found in Alias and Buenzli (2018) to be a curvature-dependent loss of tissue-secreting cells,

$$A(\kappa) = -A_0\kappa, \quad (3.3)$$

and a porosity-dependent secretory rate,

$$k = a_k + b_k \sqrt{\frac{\phi}{\pi}}, \quad (3.4)$$

where $\sqrt{\phi/\pi}$ is an approximation of the pore radius R . The linear secretory rate function of R is based on experimental data, with the two parameters being $a_k = 3.2741 \times 10^{-6} \text{ mm}^2/\text{day}$, and $b_k = 8.5727 \times 10^{-5} \text{ mm}^2/\text{day}$ (Alias and Buenzli, 2018). Therefore, there are two remaining parameters to be fit to the experimental data, A_0 and D .

Equations (3.1) and (3.2) define a PDE to be solved on an evolving interface and

must be solved numerically. This problem is not trivial due to the asymmetries in the interface which result in the development of heterogeneities in cell density and nonlinearities which arise from the coupling of the interface speed with density. We choose to solve this model using a Kurganov-Tadmor (KT) finite volume method (FVM) based on computer code intially written, and kindly shared with us by Almie Alias ([Alias, 2019](#)). This choice was motivated by the conservation properties of the method and its high resolution, which are important when dealing with small-scale irregularities in initial interface ([Alias and Buenzli, 2018](#)). The KT FVM solves for the position and density of the interface in polar coordinates in conservative form, therefore the governing expressions become

$$\frac{\partial R}{\partial t} = -\frac{k\eta}{R}, \quad (3.5)$$

$$\frac{\partial}{\partial t} \left(\frac{\partial R}{\partial \theta} \right) + \frac{\partial}{\partial \theta} \left(\frac{k\eta}{R} \right) = 0, \quad (3.6)$$

$$\frac{\partial(\eta)}{\partial t} + \frac{\partial}{\partial \theta} \left[\frac{k\eta^2 \frac{\partial R}{\partial \theta}}{R \left(R^2 + \left(\frac{\partial R}{\partial \theta} \right)^2 \right)} + D \left(\frac{\eta \frac{\partial R}{\partial \theta} \left(R + \frac{\partial R}{\partial \theta} \right)}{\left(R^2 + \left(\frac{\partial R}{\partial \theta} \right)^2 \right)^2} - \frac{\frac{\partial \eta}{\partial \theta}}{R^2 + \left(\frac{\partial R}{\partial \theta} \right)^2} \right) \right] \quad (3.7)$$

$$= -A\eta - Otk\eta,$$

where $g = R\sqrt{1 + 1/R^2(\partial R/\partial \theta)^2}$ is the surface metric and $\eta = \rho g$ is the cell density per unit angle ([Alias and Buenzli, 2017](#)). The initial density of osteoblasts is taken to be a uniform $\rho_0 = 161$ cells/mm ([Marotti et al., 1976](#); [Alias and Buenzli, 2018](#)). Further details on the KT FVM scheme can be found at [Alias \(2019\)](#).

3.2 Parameter Sweep

To determine the values of D and A_0 which best reproduce the final condition from the experimental data, simulations are run for all eight experimental os-

A_0 (mm/day)	0.000605, 0.0009075, 0.00121 , 0.0015125, 0.001815
D (mm ² /day)	0.000375, 0.0005625, 0.00075 , 0.0009375, 0.001125

Table 3.1: Parameter Sweep Values

teons with varying D and A_0 values around the values used in [Alias and Buenzli \(2018\)](#), that is $A_0 = 0.00121$ mm/day and $D = 0.00075$ mm²/day. The lower and upper bounds for the parameter sweep are taken to be $\pm 50\%$ of the above values. The parameter sweep values are listed in Table 3.1. Therefore, there is a 5×5 grid of parameter pairs to test for each of the 8 osteons, resulting in a total of 200 simulations to be run.

As the loss of secreting cells is a function of curvature ($A(\kappa)$), this function is first re-scaled by a factor α for each osteon such that $\alpha A(\langle \kappa_0 \rangle) = A_0$ where $\langle \kappa_0 \rangle$ indicates the average curvature around the pore at time 0. This ensures that smaller osteons do not start infilling with a higher rate of loss of secreting cell than larger osteons. Furthermore, the simulations are stopped when the target remaining pore area (that of the Haversian canal in the experimental osteon) is reached.

To find the parameters that best recreate the final pore of the experimental data, (\bar{A}_0, \bar{D}) , error metrics are defined to compare the final states of the bone pore in the experimental data and in the simulation results. To illustrate the results, an example simulation output for one osteon is compared to experimental data in Figure 3.3. The difference in final pore includes differences in area, location, shape, and orientation. To capture these properties mathematically, we consider the spatial distribution which describes the final pore shape and examine the zeroth, first, and second moments of this distribution. This distribution is

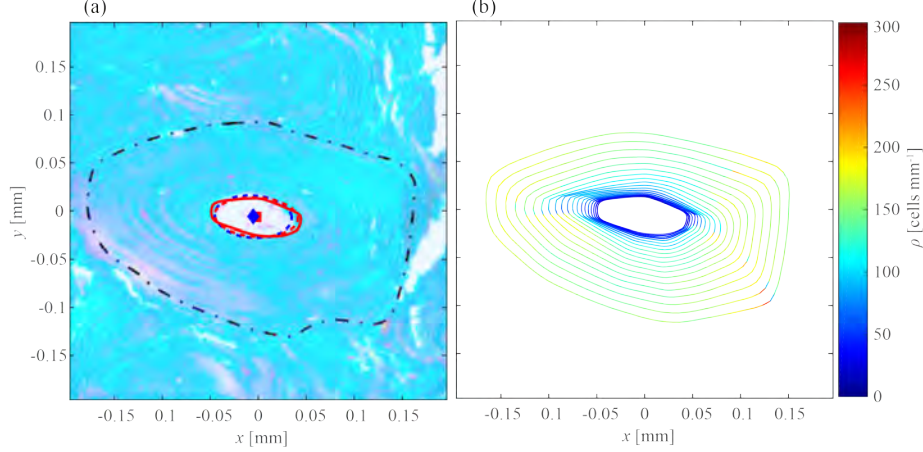


Figure 3.3: Experimental data (a) compared with results from one simulation (b). In (a), the ellipse fit to the final experimental pore shape is indicated with a blue dashed line and the centroid of the final experimental pore is shown with a blue diamond. The red solid line indicates the final pore shape from the simulation, the red dashed line is the ellipse fit to this shape, and the red square is the centroid of the final pore from the simulation results. The parameter values for this simulation are $A_0 = 1.51 \times 10^{-3}$ mm/day and $D = 1.125 \times 10^{-3}$ mm²/day

an indicator function of the pore area defined as

$$\chi_{\mathcal{A}}(\mathbf{r}) = \begin{cases} 1 & \mathbf{r} \in \mathcal{A} \\ 0 & \text{otherwise,} \end{cases} \quad (3.8)$$

where \mathbf{r} is a vector indicating position and \mathcal{A} is the remaining pore area. The zeroth moment of this distribution corresponds to the pore area, the first moment to the centroid of the pore, and the second moment to the ellipse which best fits the pore shape. We calculate these properties on both the experimental final pore (Haversian canal) and on the final pore of the model output to define error metrics. The difference in the final density distribution of osteoblasts is described by averaging osteoblast density around the interface. In total, we define five error metrics, based on discrepancies in

1. Cell density;
2. Pore area;
3. Centroid of the pore;
4. Pore orientation; and
5. Pore aspect ratio.

Cell density

A reasonable assumption for the average density of osteoblasts at the end of osteon infilling is $\rho_{\text{exp}} = 46$ cells/mm (Marotti et al., 1976; Buenzli, 2014). We define the error in density as the relative error between the expected final density of osteoblasts and the mean density in the simulation data at the final time,

$$\epsilon_{\rho}^i = \frac{|\rho_{\text{exp}} - \langle \rho_{\text{sim}}^i \rangle|}{\rho_{\text{exp}}}, \quad \text{where} \quad \langle \rho_{\text{sim}}^i \rangle = \frac{1}{\mathcal{A}^i} \oint_{\partial\mathcal{A}^i} \rho_{\text{sim}}^i dl, \quad (3.9)$$

and the subscript ‘sim’ indicates the simulation data, the subscript ‘exp’ indicates experimental data, and the superscript ‘ i ’ indicates the i^{th} osteon ($i = 1, \dots, 8$).

Pore area

The second error metric considered is the relative error of the final pore area, determined as the zeroth moment of $\chi_{\mathcal{A}}(\mathbf{r})$, i.e. the area is $\mathcal{A} = \iint \chi_{\mathcal{A}}(\mathbf{r}) dx dy$,

$$\epsilon_{\mathcal{A}}^i = \frac{|\mathcal{A}_{\text{exp}}^i - \mathcal{A}_{\text{sim}}^i|}{\mathcal{A}_{\text{exp}}^i}. \quad (3.10)$$

It is important to note that the simulations are stopped when the remaining pore area matches that of the experimental data, therefore $\epsilon_{\mathcal{A}}^i$ is only non-zero when the target area is not reached, for example if the depletion rate of osteoblasts is too high.

Centroid of the pore

The centroid of $\chi_{\mathcal{A}}(\mathbf{r})$ is defined as

$$\mathbf{r}_c = \langle \mathbf{r} \rangle = \frac{\iint \mathbf{r} \chi_{\mathcal{A}}(\mathbf{r}) dx dy}{\iint \chi_{\mathcal{A}}(\mathbf{r}) dx dy}. \quad (3.11)$$

Since the finite volume solver stores the interface and the osteoblast density in polar coordinates, the centroid is calculated by approximating the following integrals using the trapezoidal rule,

$$\begin{bmatrix} \langle x \rangle \\ \langle y \rangle \end{bmatrix} = \frac{1}{\int_0^{2\pi} d\theta \int_0^{R(\theta)} dr r} \begin{bmatrix} \int_0^{2\pi} d\theta \int_0^{R(\theta)} dr r^2 \cos(\theta) \\ \int_0^{2\pi} d\theta \int_0^{R(\theta)} dr r^2 \sin(\theta) \end{bmatrix}, \quad (3.12)$$

where $R(\theta)$ is the radius of the pore at angle θ . The error metric on the location of the final pore is defined as

$$\epsilon_c^i = \frac{\|\mathbf{r}_{c_{\text{exp}}}^i - \mathbf{r}_{c_{\text{sim}}}^i\|}{\sqrt{\mathcal{A}_{0_{\text{exp}}}^i}}, \quad (3.13)$$

where $\|\cdot\|$ indicates the two-norm, and $\mathcal{A}_{0_{\text{exp}}}^i$ is the initial pore area in the i^{th} experimental data osteon, which is used as a normalising factor across osteons.

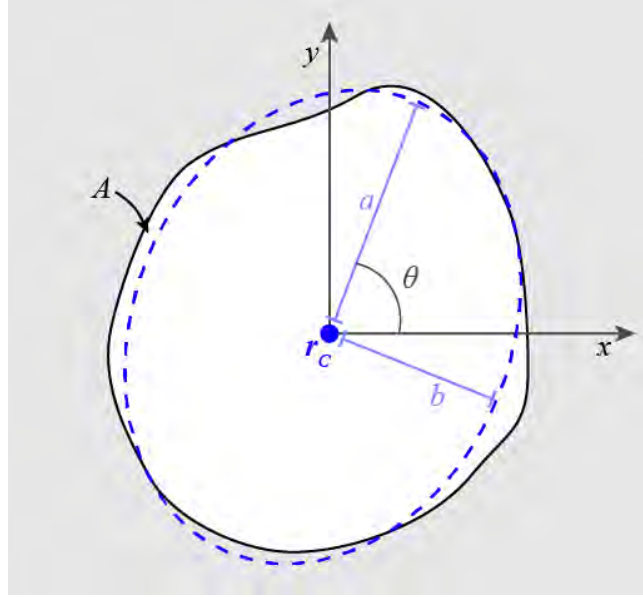


Figure 3.4: Zeroth, first, and second moments of pore indicator function. Note that origin of xy axis is aligned with \mathbf{r}_C to clarify θ , this is not the case in the simulation results.

Pore shape

The second moments of the spatial distribution of the pore define elements of a covariance matrix, S , where

$$S = \begin{bmatrix} \langle (x - \langle x \rangle)^2 \rangle & \langle (x - \langle x \rangle)(y - \langle y \rangle) \rangle \\ \langle (x - \langle x \rangle)(y - \langle y \rangle) \rangle & \langle (y - \langle y \rangle)^2 \rangle \end{bmatrix}. \quad (3.14)$$

This matrix can be used to describe the ellipse which best fits the pore shape such that $(\mathbf{r} - \mathbf{r}_C)^\top S(\mathbf{r} - \mathbf{r}_C) = 1$ (Figure 3.4). That is, the equation for the ellipse in general form is given by $S_{11}(x - x_C)^2 + 2S_{12}(x - x_C)(y - y_C) + S_{22}(y - y_C)^2 = 1$. Given the covariance matrix S , the orientation of the ellipse, θ , as well as the ratio between its major and minor axes can be calculated. The length of the major axis, a , and the minor axis, b of the ellipse are given by the eigenvalues

S , where $b \leq a$. The orientation of the ellipse, defined as the angle between the positive x -axis and the major ellipse axis, can be obtained by the orthogonal transformation that makes S diagonal. That is,

$$S = R^{-1}DR, \quad (3.15)$$

where

$$D = \begin{bmatrix} a & 0 \\ 0 & b \end{bmatrix}, \quad (3.16)$$

and R is the transformation of axes required. The calculation of R is not explicitly needed for find θ , the orientation of the ellipse is given by

$$\theta = \frac{1}{2} \arctan \left(-\frac{2S_{12}}{S_{22} - S_{11}} \right). \quad (3.17)$$

The properties of the ellipse of interest are annotated in Figure 3.4. This provides us with two error metrics on the shape of the final pore, defined as the relative error between the experimental data and the simulation data of the ellipse orientation, θ and axis ratio, $\mathcal{R} = b/a$:

$$\epsilon_\theta^i = \frac{|\theta_{\text{exp}}^i - \theta_{\text{sim}}^i|}{\theta_{\text{exp}}^i}, \quad (3.18)$$

$$\epsilon_{\mathcal{R}}^i = \frac{|\mathcal{R}_{\text{exp}}^i - \mathcal{R}_{\text{sim}}^i|}{\mathcal{R}_{\text{sim}}^i}. \quad (3.19)$$

Total error

Finally, to provide a single measure of error between the experimental data and simulation results, the total error metric for a single osteon simulation with parameter pair (A_0, D) is defined as the sum of Equations (3.9), (3.10), (3.13),

(3.18), and (3.19),

$$\epsilon_{\text{total}}^i = \epsilon_{\rho}^i + \epsilon_{\mathcal{A}}^i + \epsilon_{\mathcal{C}}^i + \epsilon_{\theta}^i + \epsilon_{\mathcal{R}}^i. \quad (3.20)$$

The total error for a given parameter pair (A_0, D) is taken to be the sum of the total errors for each osteon,

$$\epsilon_{\text{total}} = \sum_{i=1}^8 \epsilon_{\text{total}}^i. \quad (3.21)$$

The aim of the parameter sweep is to find the parameter pair (\bar{A}_0, \bar{D}) with the smallest total error metric across all osteons.

4 Results

The error surfaces produced by each metric from the parameter sweep are presented in Figure 3.5, with the total error surface presented in Figure 3.6. Separating the different error metrics shows that the area and density error metrics have opposing behaviour as a function of different A_0 values. That is, high A_0 values reduce the density error but increase the area error and vice versa (Figure 3.5).

The centroid error shows more sensitivity to the diffusivity value than the area and density metrics. However, the magnitudes of the individual relative error metrics are quite different, therefore once they are considered together in the total error metric, the area and density metrics are most significant. The total error metric is lowest at the center value of A_0 (1.21×10^{-3} mm/day) and is slightly lower at higher diffusivities (Figure 3.6). As the difference along the diffusivity axis is small, perhaps a wider range of diffusivities should be explored. The apparent lack of sensitivity to diffusivity may be because only one error metric is evaluating density, and ϵ_{ρ} does not include a measure of density het-

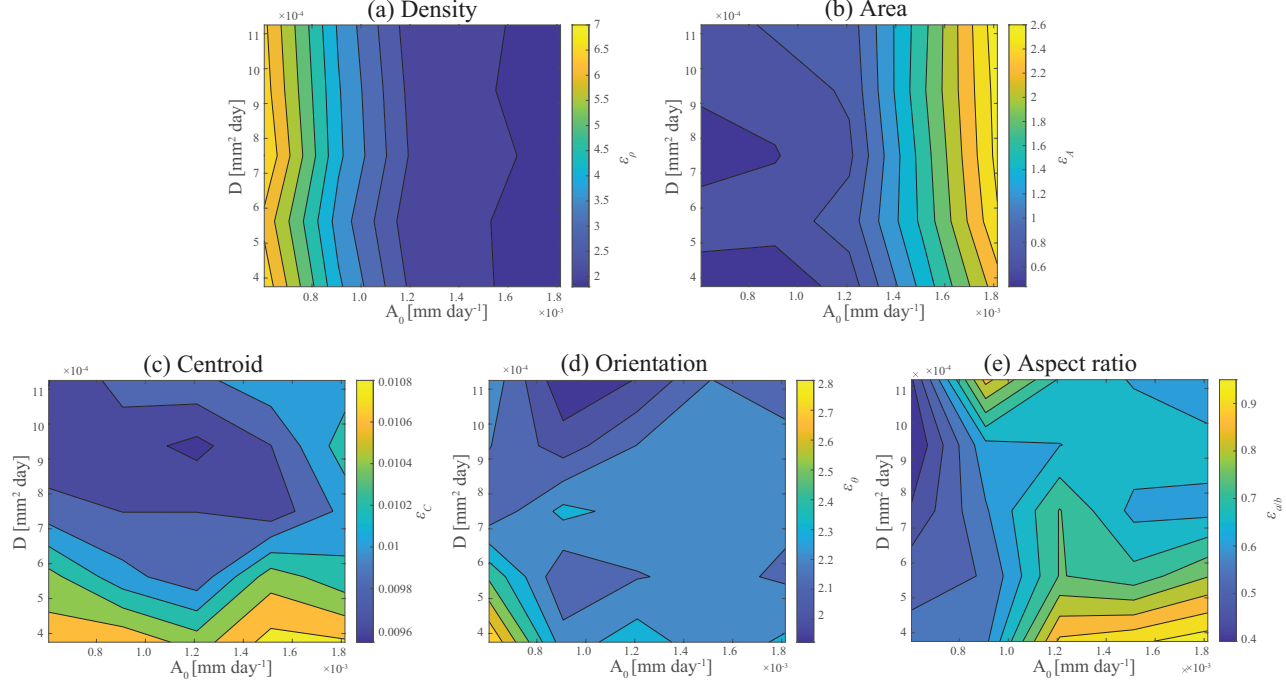


Figure 3.5: Individual error metrics from the parameter sweep.

erogeneticities along the final pore interface, only the average density at the final time point. As can be seen in Figure 3.7, there can be significant differences in density around the interface for the same value of A_0 . If data was available about the heterogeneities in density around the interface, the sensitivity of more detailed error metrics of density to diffusivity may become more apparent. Therefore, we can conclude that $\bar{A}_0 = 1.21 \times 10^{-3}$ mm/day and that the range of D values considered is appropriate, $\bar{D} \in [3.75 \times 10^{-4}, 1.125 \times 10^{-3}]$ mm 2 /day (Figure 3.6). In general, the simulations using (\bar{A}_0, \bar{D}) agree well with the data qualitatively (Figure 3.8).

The parameter sweep results show that the values of A_0 and D proposed in Alias and Buerzli (2018) are reasonable in view of the error metrics defined

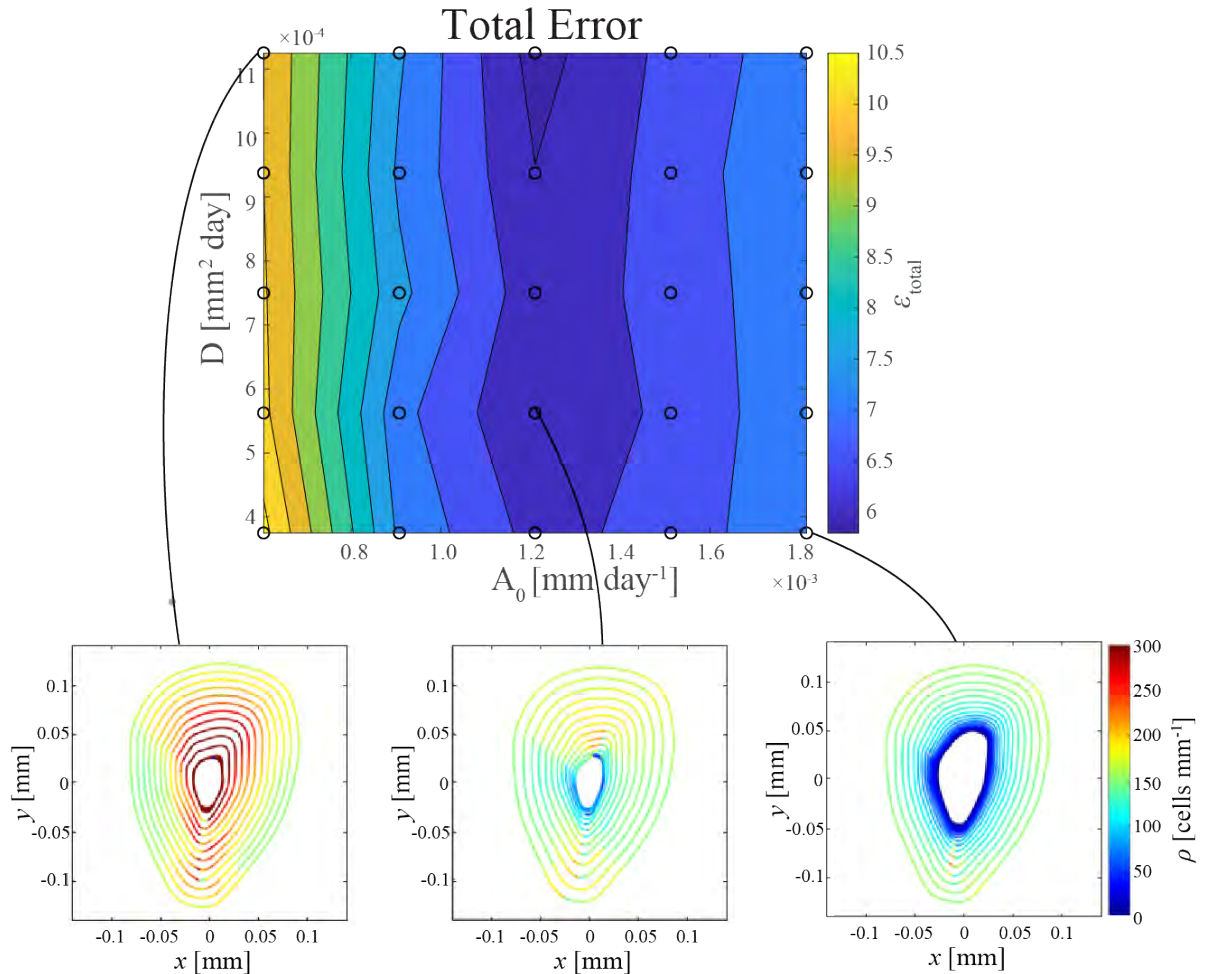


Figure 3.6: Total error metric for parameter sweep with some results from one osteon highlighted.

here for the experimental osteons. In [Alias and Buenzli \(2018\)](#), these A_0 and D values were based solely on achieving smooth, circular final pores, and not on the comparison with experimental data. Our parametric study which calibrates A_0 and D to experimental data therefore suggests that the geometric dependence of osteoblast behaviour encapsulated in $A(k)$ and $k(\phi)$ has the effect to efficiently smooth the bone interface and to lead to round, regular final pores.

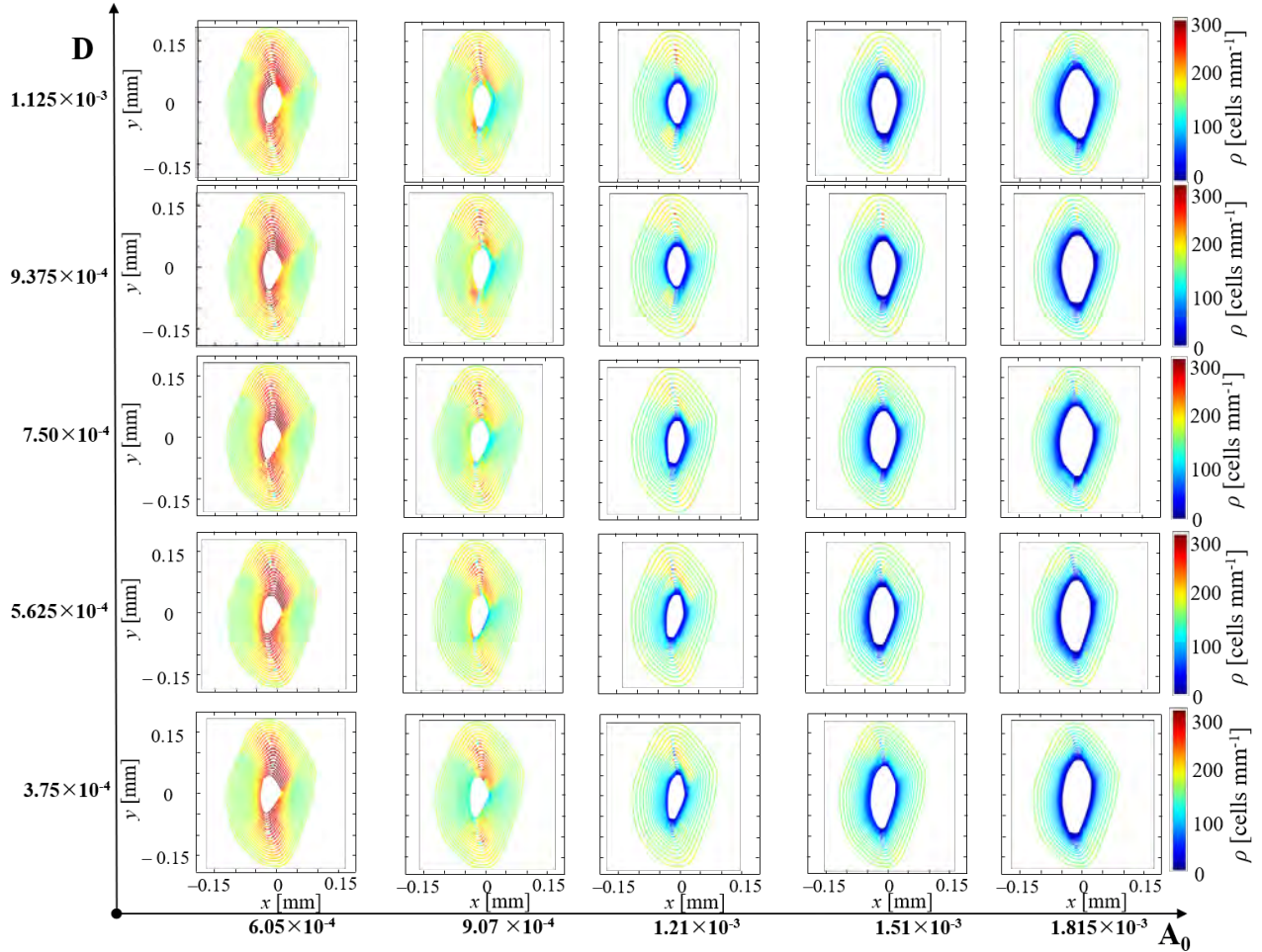


Figure 3.7: All simulation results for one osteon.

There is a large difference in magnitude across the different error metrics. These magnitude differences are deemed to be important, as a seven-fold increase in expected osteoblast density is more important to avoid than a slight difference in the orientation of the pore. Therefore, we simply take the sum of all five metrics. However, a weighting of the metrics could be considered if biologically relevant, for example, if one had more confidence about data relating to one

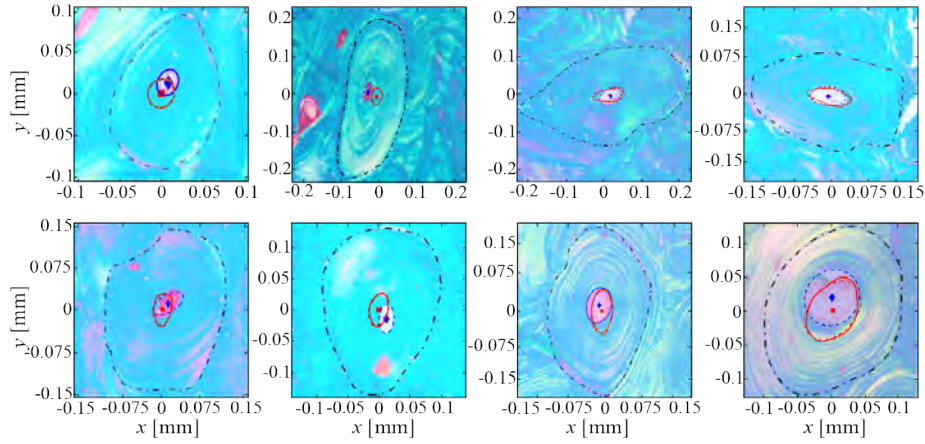


Figure 3.8: Results for optimal parameters (\bar{A}_0, \bar{D}) for each osteon. The centroid of the experimental data pore is denoted by a blue diamond and the fitted ellipse to the experimental data is a blue dashed line. The red square denotes the centroid of the simulation results, the red solid line is the experimental final pore and the red dotted line is the ellipse fitted to the simulation results.

error metric than another.

4.1 Osteons with off-center Haversian canals

Having been able to reproduce osteon features well for reasonably regular pores, the final aim of this study is to apply the model to pores with off-centered Haversian canals. We aim to gain insight into osteoblast behaviours which may cause these osteons to develop. Figure 3.9 shows the difference between an osteon where the Haversian canal is centered within the cement line, and an osteon where the Haversian canal is not in the center of the cement line. It is clear from this comparison that further mechanisms are present which lead to the location of the final pore being significantly off-center. Although we can see in Figure 3.9 some influence of neighbouring osteons on the cement line, these irregularities can be smoothed by the curvature-control model with the final pore remaining in the center. The off-centering of the pore requires more mechanisms than curvature control. We investigate three hypotheses which could lead to osteons with off-center final pores:

- H1.* A time delay in the commencement of new tissue secretion on a portion of the initial interface;
- H2.* A nonuniform initial density of osteoblasts which causes faster infilling on one portion of the osteon interface; and
- H3.* A spatially-dependent nonuniform secretory rate such that one region infills faster than the rest.

The time delay of *H1* is implemented by setting $k = 0 \text{ mm/day}$ for $y > 0 \text{ mm}$ for $t < 10 \text{ days}$. The value of 10 days is chosen by inspecting the biological image and noticing the ‘eclipsing’ lamellae about one third of the way through the infilling process. *H2* is applied by changing the initial uniform density of osteoblasts ($\rho_0 = 161 \text{ cells/mm}^3$) to be a sinusoidal initial density function of θ , with values centered around ρ_0 . The value of ρ_0 is obtained from the parameter

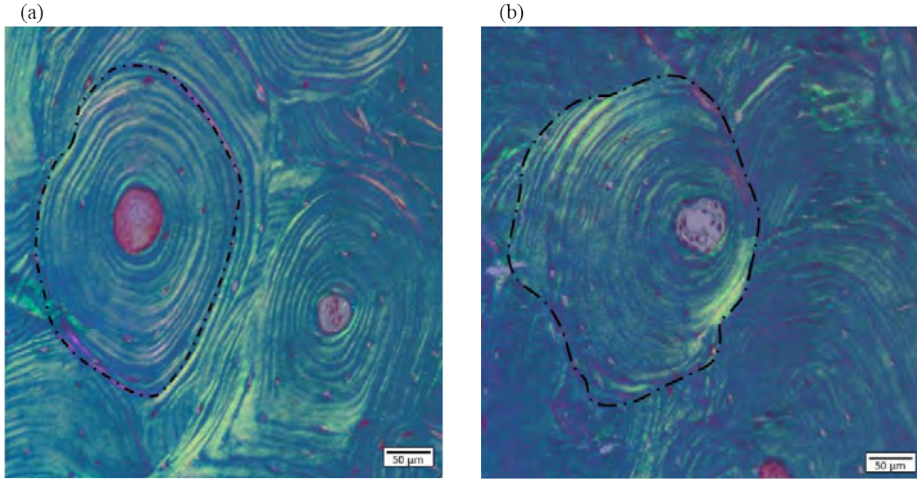


Figure 3.9: Experimental data images showing osteons with centered Haversian canals (a) and off-centered canals (b).

study conducted in Alias and Buerzli (2018). Therefore, there is the same total number of cells around the initial interface as when a uniform initial cell density is used. A similar strategy is used for $H3$, where the k values are sinusoidally perturbed as a function of θ and the center value is taken from the parametric study in Alias and Buerzli (2018). We apply the three mechanisms to the osteon shown in Figure 3.10 and begin to analyse differences between the infilling behaviours.

All three hypotheses successfully create an off-center final pore. Simulations performed under $H1$ show ‘eclipsing’ lamellae behaviour, that is, lamellae which do not reach entirely around the osteon, but rather narrow out to join with other lamellae. This behaviour can be observed in the experimental osteon (Figure 3.10a). Furthermore, cell density around the final pore under $H1$ is close to the final density expected from experimental data after the osteon has been infilled. Figures 3.10b and c show that under $H2$ and $H3$ the tissue evolution produces variation in thickness of individual lamellae, which has been noted

by our collaborators as an important property. In Figure 3.10b (*H*₂), a high density of osteoblasts can be seen for most of the simulation for $y < 0$ between $x \pm 0.05\text{mm}$. Further experimental data about osteoblast density throughout infilling is needed to confirm whether such high values of cell density as seen in *H*₂ are possible during bone formation. Cell density results for *H*₃ are more homogeneous, however the shape of the final pore is less aligned with the experimental data.

The differences between *H*₂ and *H*₃ show the importance of the coupling of density and interface velocity. Initially, changing either the secretory rate or the density has the same effect on the interface velocity, however due to the dependence of the interface velocity on the solution of the density evolution equation, significantly different behaviour is seen in Figures 3.10b and c. This shows the importance of considering secretory rate and cell density independently. These simulations suggest that cell density information over time could help understand what underlying mechanisms are responsible for the generation of off-center Haversian canals.

This short exploration into the generation of off-center Haversian canals in osteons has shown that experimentally, we can look for eclipsing behaviour, lamellar thickness, and cell density to understand which of the three possible mechanisms is responsible for the asymmetry.

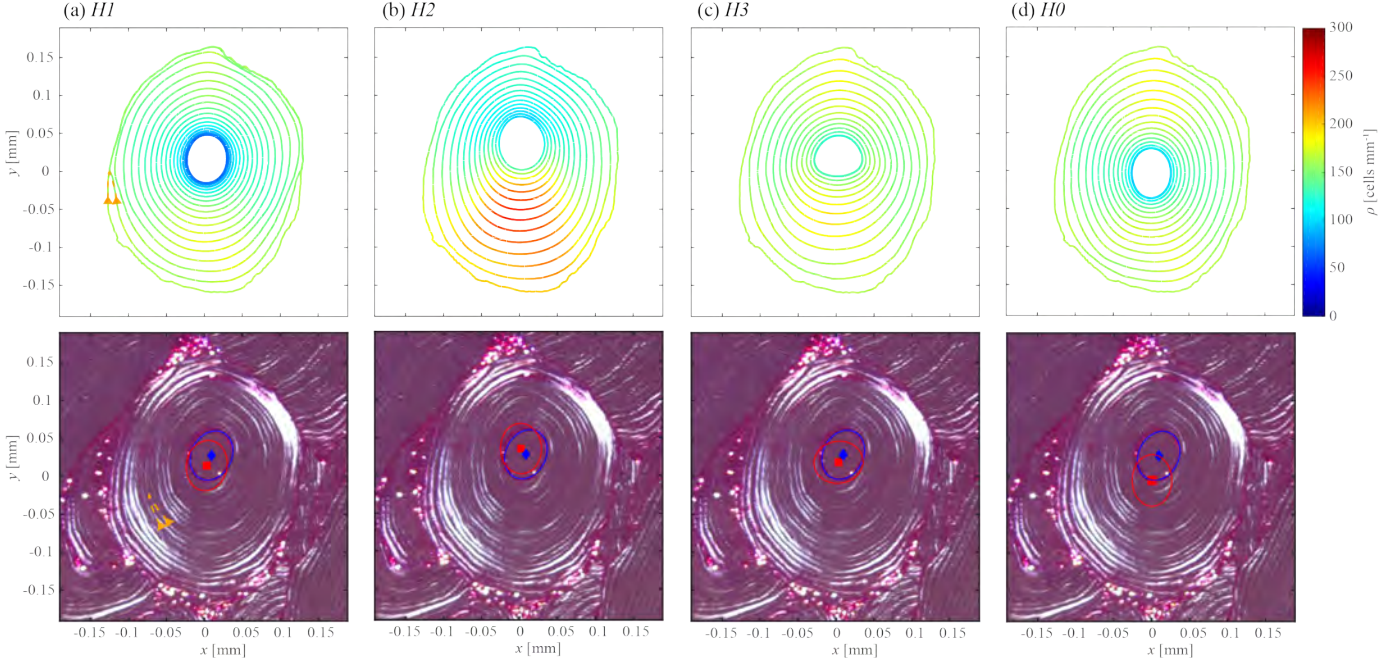


Figure 3.10: Results of simulations of osteon with off-centered Haversian canal, with simulation results at distinct time point above and the final pore ellipse plotted on the experimental data below. (a) shows the results under $H1$, with an example of eclipsing lamellae highlighted in orange in both the simulation and the experimental data. (b) shows the results under $H2$. (c) shows the results under $H3$. (d) shows the results under $H0$, where no mechanisms are added to off-center the final pore.

4.2 Numerical solver issues

The investigation of the osteons with off-center final pores brought to light some numerical issues using the KT FVM. It was found that the placement of the origin in the polar coordinate framework influenced the simulation results significantly for small radii due to numerical inaccuracies. The different behaviours according to origin placement can be seen in Figure 3.11a and b, where the infilling of a perfectly circular osteon is simulated with a centered origin, and an off-centered origin. Figures 3.11c and d show how the placement of the origin of the polar coordinate system influences simulations on the osteon shown in

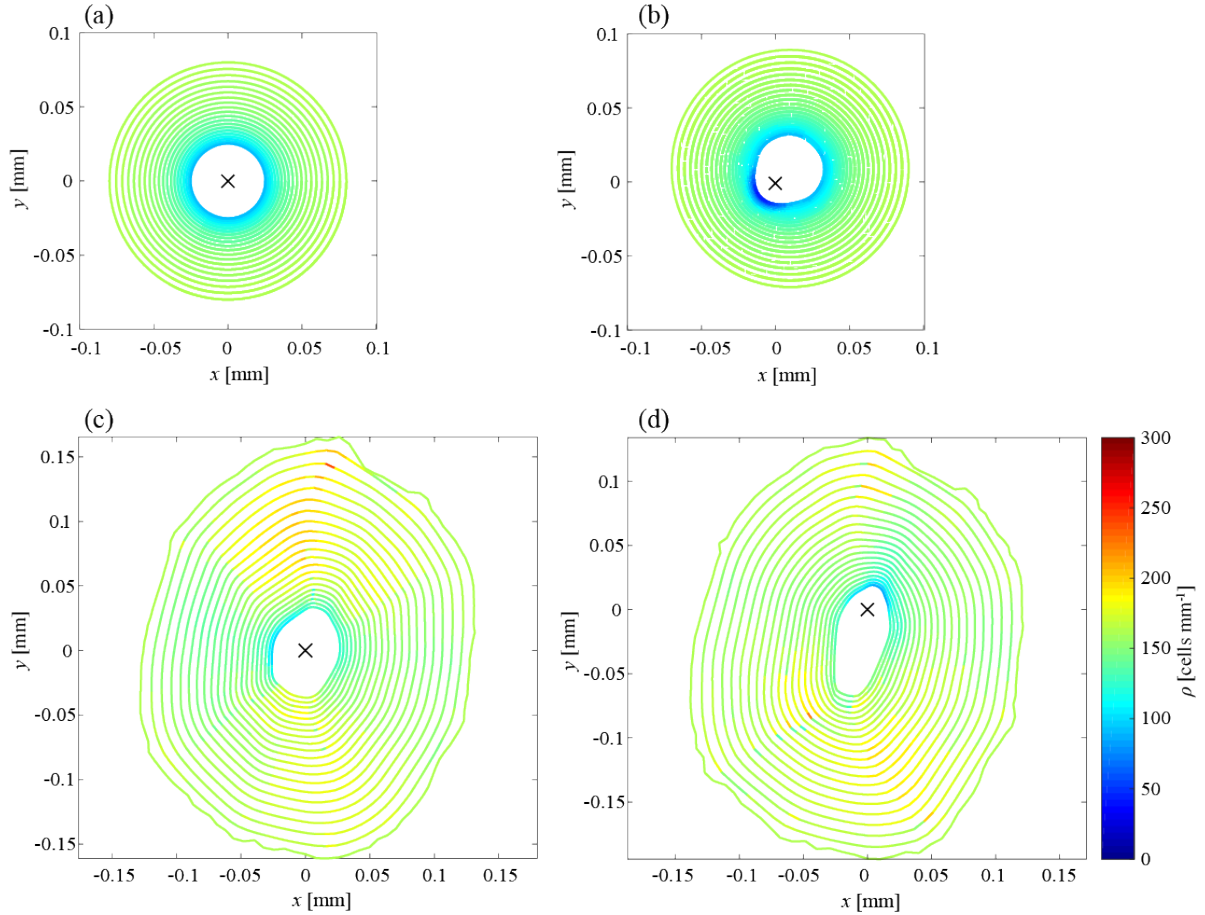


Figure 3.11: Different model results due to placement of origin in KT FVM simulations. (a) and (b) show the results with a circular pore while (c) and (d) show the results of simulations on the experimental pore used in Figure 3.10. (a) and (c) have the origin placed at the center of mass of the initial pore shape while (b) and (d) have an off-center origin.

Figure 3.10. Therefore, origin placement seems important for this numerical method, particularly when the remaining pore area is small. To alleviate this numerical inaccuracy, the origin was recentered to be at the centroid of the remaining pore periodically. The origin placement influence is an area open to further investigation.

4.3 Discussion

This chapter demonstrates the suitability of our mathematical model for analysing osteon infilling data. We propose a method of quantitative analysis for density and spatial data and conduct a parameter sweep with our devised error metric.

The parameter sweep results in the determination of reasonable parameters and suggests that more insights could be gained into diffusion if more information was available about the density of osteoblasts through the infilling process. There is potential for further quantitative analysis by identifying intermediary lamellae and comparing the simulation results at intermediate time points. This may be achieved by comparing the interface from the numerical simulation when the remaining pore area is the same as the area contained within the experimental intermediary lamellae.

We show how our mathematical model can be combined with the analysis of tissue material properties to gain insights into tissue growth behaviour. Through the analysis of the biological artefacts present in osteons with off-center Haversian canals, we are able to propose three hypotheses which can be assessed using our mathematical model. Thus the mathematical model can facilitate the understanding of atypical biological growth behaviour.

Some instability issues were found initially with the CBPM when dealing with the experimental osteon data, presumably because of small-scale irregularities in the experimental initial conditions, hence the KT FVM was used. Due to the issues of origin placement in the KT FVM, finding the best algorithm to solve the model for osteon infilling is open for further investigation. There is the potential for further exploration into the CBPM under more taxing initial

conditions, for example by implementing the local grid refinement scheme described in Leung and Zhao (2009).

Further information about cell density would benefit both the parameter sweep and the exploration into osteons with off-center Haversian canals. In order to gain more insight as to which of the three hypotheses considered is better suited to the experimental behaviour, information about the cell density around the interface throughout infilling or time information would be useful, as currently only interface position can be seen.

Chapter 4

Concluding Remarks and Outlook

The aim of this thesis was to gain insight into individual cell behaviours and overall tissue dynamics during tissue growth using mathematical modelling of biological tissue growth under curvature control and directed cell guidance. A mathematical model has been derived from conservation principles for the evolution of cell density along an evolving tissue interface under curvature control and tangential cell motion. The inclusion of tangential cell motion in the governing equations allows for many different directed cell guidance mechanisms to be modelled. The derivation of the mathematical model is in covariant form and in three dimensions and results in a PDE on a moving boundary, whose motion is coupled with the solution of the PDE. Using a hybrid front-tracking method, the CBPM, the model was solved and the implementation of this method was validated with exact solutions. The new model was compared to existing models in the literature and applied to novel biological situations where tangential motion is important. Experimental osteon infilling data was also compared to the model results and a framework of quantitative analysis was defined to compare simulation results against experimental data. After establishing the suitability of the model to osteon infilling, a case of atypical infilling behaviour was examined, illustrating the use of the mathematical model to test different hypotheses



about the biological cell behaviours which may be difficult to measure experimentally.

The mathematical model presented here has been derived under rigorous conservation principles and includes lateral cell diffusion, the crowding and spreading effect of curvature, cell tangential advection, interface tangential motion, and sink or source terms. Similar governing equations can be found in the literature in the context of surfactant mass balance in physico-chemical systems. The mathematical model derived here agrees with equations found in the literature in particular cases and the derivation clarifies some confusion in the literature about the nature of the time derivative along different trajectories (see Chapter 2 Section 2.B). The CBPM is a promising method of solving the governing equations derived herein and may provide a way of addressing the origin placement considerations needed for the KT FVM (Figure 3.11). Furthermore, the CBPM method is applicable to three dimensions, therefore there is the possibility of modelling a three dimensional bone pore and gaining insights into the intricate three-dimensional structures of Haversian canals (Cooper et al., 2006; Arhatari et al., 2011).

Through the mathematical model derived in this thesis, insight was gained into the interactions between curvature control and cell guidance mechanisms. We showed in our simulations of bone resorption (Chapter 2, Section 3.3) that only by explicitly considering both curvature control and cell guidance can we represent resorption cavities progressing through the bone tissue with a stable resorption front shape. The mathematical model has a general tangential cell advection term, hence there is flexibility in the different types of systems that can be considered. The influence of mechanical loading could be included as

a signal influencing the tangential velocity. Similarly to how a gradient field was used to model chemotaxis, a strain field such as the one presented in Smit and Burger (2000) could be used. Exploring the different types of signals is an area of future work. Furthermore, external velocity field influences could also be considered for more atypical osteon infilling behaviour, such as drifting osteons (Figure 4.1). Drifting osteons occur when there is continuous resorption on one side of the canal and continuous infilling on the other, so that the canal drifts in the cross-sectional plane (Robling and Stout, 1999). Examining structurally mature drifting osteons, the directions of the resorption canal movement may be extracted (Robling and Stout, 1999). Using the model derived in this thesis, tangential cell motion could be used to test these theories about drifting osteons involving resorption canal movement in the cross-sectional plane presented in Robling and Stout (1999) and Maggiano (2012).

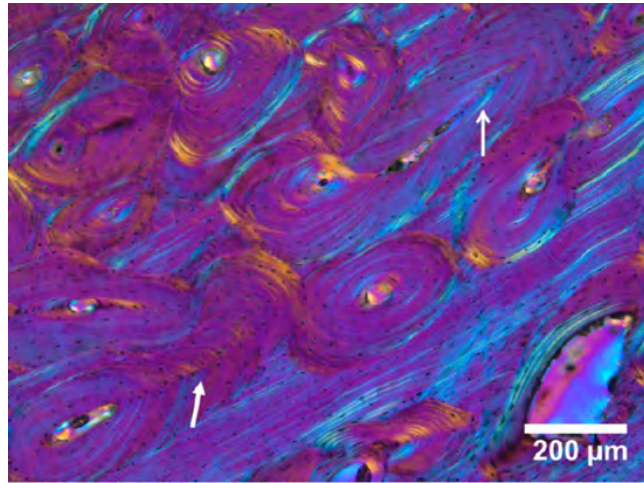


Figure 4.1: Drifting osteons (arrows), reproduced with permissions from Maggiano (2012)

Tissue properties and tissue material anisotropies can be analysed using the mathematical model to gain insights into cell behaviour during tissue evolution.

tion. Biological artefacts in the osteon tissue have been used in conjunction with the model to evaluate hypotheses about the generation of atypical tissues (Section 4.1). It has also been established that tangential cell motion during infilling could lead to anisotropies in tissue material properties, more specifically in collagen fibre orientation. In our exploration, the mechanisms of tissue material creation were not explicitly considered. The mathematical model derived here could be coupled with a model for the generation of tissue material properties to gain more insights into cell behaviour and the dynamics of anisotropic material property creation. Such models exist in wound healing (Cumming et al., 2010) where the creation and destruction of tissue material is modelled using bulk and surface mass balance.

As well as qualitative inspection of tissues, methods of quantitative analysis have been developed. Fitting ellipses to both the experimental data and simulations of osteon pores enabled a quantitative comparison of the pore shapes. The parameter sweep in Section 3.2 allowed for justification of model parameters and highlighted that additional information about the density of osteoblasts throughout infilling is required. Now that quantitative comparison metrics have been established, it could be possible to carry out uncertainty quantification of the model parameters. This could be achieved with methods such as Approximate Bayesian Computation. Our collaborators are currently working on new experimental data analysis techniques to extract cell density information. This additional data will be useful in further studies to investigate the three different hypotheses examined in Section 4.1.

In conclusion, the mathematical model developed in this thesis has highlighted the importance of considering curvature control and directed cell guidance mech-

anisms in analysing the development of biological tissues. This mathematical modelling has helped gain insights into the behaviours of osteoblasts and osteoclasts during the bone remodelling process and provides a basis into further explorations of the spatial organisation of tissue material anisotropies as well as the mechanisms which cause atypical bone remodelling behaviour.

Bibliography

- Alias, M.A. 2019. Mathematical Modelling of the Geometric Control of Bone Tissue Growth. Monash University. <https://doi.org/10.4225/03/5aa082aa5ebb9>
- Alias, M. A. and Buenzli. P. R. 2017. Modeling the Effect of Curvature on the Collective Behavior of Cells Growing New Tissue. Biophysical Journal, 112, 193-204. <https://doi.org/10.1016/j.bpj.2016.11.3203>
- Alias, M. A. and Buenzli. P. R. 2018. Osteoblasts infill irregular pores under curvature and porosity controls: a hypothesis-testing analysis of cell behaviours. Biomechanics and Modeling in Mechanobiology, 17, 1357–1371. <https://doi.org/10.1007/s10237-018-1031-x>
- Alias, M. A. and Buenzli, P. 2019. A level-set method for the evolution of cells and tissue during curvature-controlled growth. International Journal for Numerical Methods in Biomedical Engineering, 36(1), e3279. <https://doi.org/10.1002/cnm.3279>
- Ambrosi, D., Ben Amar, M., Cyron, C., Desimone, A., Goriely, A., Humphrey, J., and Kuhl, E. 2019. Growth and remodelling of living tissues: perspectives, challenges and opportunities. Journal of the Royal Society, Interface, 16(157), 20190233. <https://doi.org/10.1098/rsif.2019.0233>
- Andreasen, C., Delaisse, J., van Der Eerden, B., van Leeuwen, J., Ding, M., and Andersen, T. 2018. Understanding age-induced cortical porosity in women: Is

a negative BMU balance in quiescent osteons a major contributor? *Bone*, 117, 70–82. <https://doi.org/10.1016/j.bone.2018.09.011>

Arhatari, B., Cooper, D., Thomas, C., Clement, J., and Peele, A. 2011. Imaging the 3d structure of secondary osteons in human cortical bone using phase-retrieval tomography. *Physics in Medicine and Biology*, 56(16), 5265–5274. <https://doi.org/10.1088/0031-9155/56/16/012>

Arnoldus, H. 2006. Conservation of charge at an interface. *Optics Communications*, 265(1), 52–59. <https://doi.org/10.1016/j.optcom.2006.03.024>

Batchelor, G. K. 1967. *An Introduction to Fluid Dynamics*. Cambridge U.P., Cambridge.

Berger, M. 2003. *A Panoramic View of Riemannian Geometry*. Springer, Berlin.

Bidan, C., Kommareddy, K., Rumpler, M., Kollmannsberger, P., Bréchet, Y., Fratzl, P., Dunlop, J., and Roeder, R. 2012. How Linear Tension Converts to Curvature: Geometric Control of Bone Tissue Growth (Geometric Control of Bone Tissue Growth). *PLoS ONE*, 7(5), e36336. <https://doi.org/10.1371/journal.pone.0036336>

Bidan C.M., Kommareddy K.P., Rumpler M., Kollmannsberger P., Fratzl P., and Dunlop J.W. 2015. Geometry as a factor for tissue growth: towards shape optimization of tissue engineering scaffolds. *Advanced Healthcare Materials*, 2(1), 186–194. <https://doi.org/10.1002/adhm.201200159>

Bidan C.M., Kollmannsberger P., Gering V., Ehrig S., Joly P., Petersen A., Vogel V., Fratzl P., and Dunlop J.W. 2016. Gradual conversion of cellular stress patterns into pre-stressed matrix architecture during in vitro tissue growth. *Journal of the Royal Society Interface*, 13(118). <https://doi.org/10.1098/rsif.2016.0136>

- Buckberry, J. and Chamberlain, A. 2002. Age estimation from the auricular surface of the ilium: a revised method. *American Journal of Physical Anthropology*, 119(3), 231–239. <https://doi.org/10.1002/ajpa.10130>.
- Buenzli, P., Pivonka, P., Gardiner, B., Smith, D., Dunstan, C., and Mundy, G. 2010. Theoretical analysis of the spatio-temporal structure of bone multicellular units. *IOP Conference Series: Materials Science and Engineering*, 10(1), 10. <https://doi.org/10.1088/1757-899X/10/1/012132>
- Buenzli, P., Pivonka, P., and Smith, D. 2011. Spatio-temporal structure of cell distribution in cortical Bone Multicellular Units: A mathematical model. *Bone*, 48(4), 918–926. <https://doi.org/10.1016/j.bone.2010.12.009>
- Buenzli, P., Pivonka, P., and Smith, D. 2014. Bone refilling in cortical basic multicellular units: Insights into tetracycline double labelling from a computational model. *Biomechanics and Modeling in Mechanobiology*, 13(1), 185–203. <https://doi.org/10.1007/s10237-013-0495-y>
- Buenzli, P. 2015. Osteocytes as a record of bone formation dynamics: A mathematical model of osteocyte generation in bone matrix. *Journal of Theoretical Biology*, 364, 418–427. <https://doi.org/10.1016/j.jtbi.2014.09.028>
- Buenzli, P. 2016. Governing Equations of Tissue Modelling and Remodelling: A Unified Generalised Description of Surface and Bulk Balance. *PLoS One*, 11(4), e0152582. <https://doi.org/10.1371/journal.pone.0152582>
- Buenzli, P., Jeon, J., Pivonka, P., Smith, D., and Cummings, P. 2012. Investigation of bone resorption within a cortical basic multicellular unit using a lattice-based computational model. *Bone*, 50(1), 378–389. <https://doi.org/10.1016/j.bone.2011.10.021>
- Buenzli, P., Lanaro, M., Wong, C., McLaughlin, M., Allenby, M., Woodruff,

M., and Simpson, M. 2020. Cell proliferation and migration explain pore bridging dynamics in 3D printed scaffolds of different pore size. In Press, *Acta Biomaterialia*. BioRxiv. <https://doi.org/10.1101/2020.03.12.989053>

Burger, E., Klein-Nulend, J., and Smit, T. 2003. Strain-derived canalicular fluid flow regulates osteoclast activity in a remodelling osteon—a proposal. Journal of Biomechanics, 36(10), 1453–1459. [https://doi.org/10.1016/S0021-9290\(03\)00126-X](https://doi.org/10.1016/S0021-9290(03)00126-X)

Cai, A.Q., Landman, K.A., and Hughes, B.D. 2007. Multi-scale modeling of a wound-healing cell migration assay. Journal of Theoretical Biology, 245, 576–594.

Callens, S.J.P., Uyttendaele, R.J.C., Fratila-Apachitei, L.E., and Zadpoor, A.A. 2020. Substrate curvature as a cue to guide spatiotemporal cell and tissue organization. Biomaterials, 232, 1-22. <https://doi.org/10.1016/j.biomaterials.2019.119739>

Chaudhuri O., Gu L., Klumpers D., Darnell M., Bencherif S.A., Weaver J.C., Huebsch N., Lee H.-p., Lippens E., and Duda G.N. 2016. Hydrogels with tunable stress relaxation regulate stem cell fate and activity. Nature Materials, 15(3), 326–334. <https://doi.org/10.1038/nmat4489>

Cooper, D., Thomas, C., Clement, J., and Hallgrímsson, B. 2006. Three-dimensional microcomputed tomography imaging of basic multicellular unit-related resorption spaces in human cortical bone. Anatomical Record Part A: Discoveries in Molecular, Cellular, and Evolutionary Biology, 288(7), 806–816. <https://doi.org/10.1002/ar.a.20344>

Cumming, B.D., McElwain, D.L.S., and Upton, Z. 2010. A mathematical model of wound healing and subsequent scarring. Journal of the Royal Society Interface, 7, 19-34.

- Curtis, A. S., and Varde, M. 1964. Control of cell behavior: topological factors. *Journal of the National Cancer Institute*, 33(1), 15–26. <https://doi.org/10.1093/jnci/33.1.15>
- Davies, J. (2013). Mechanisms of morphogenesis (2nd ed.). Academic Press, Amsterdam.
- Deligianni, D. D., Katsala N. D., and Missirlis Y. F. 2001. Effect of surface roughness of hydroxyapatite on human bone marrow cell adhesion, proliferation, differentiation and detachment strength. *Biomaterials*, 22, 87–96. [https://doi.org/10.1016/S0142-9612\(00\)00174-5](https://doi.org/10.1016/S0142-9612(00)00174-5)
- Discher D.E., Janmey P., and Wang Y.-l. 2005. Tissue cells feel and respond to the stiffness of their substrate. *Science*, 310 (5751), 1139–1143. <https://doi.org/10.1126/science.1116995>
- Du, J., Fix, B., Glimm, J., Jia, X., Li, X., Li, Y., and Wu, L. 2006. A simple package for front tracking. *Journal of Computational Physics*, 213, 613–628.
- Dzobo, K., Thomford N.E., Senthebane D.A., Shipanga H., Rowe A., Dandara C., Pillay M., and Motaung K.S. 2018. Advances in Regenerative Medicine and Tissue Engineering: Innovation and Transformation of Medicine. *Stem Cells International*, 2018, 2495848. <https://doi.org/10.1155/2018/2495848>
- Ehrig, S., Schamberger, B., Bidan, C., West, A., Jacobi, C., Lam, K., Kollmannsberger, P., Petersen, A., Tomancak, P., Kommareddy K, Fischer F.D., Fratzl, P., and Dunlop, J. 2019. Surface tension determines tissue shape and growth kinetics. *Science Advances*, 5(9), eaav9394. <https://doi.org/10.1126/sciadv.aav9394>
- Engler A.J., Sen S., Sweeney H.L., and Discher D.E. 2006. Matrix elasticity

directs stem cell lineage specification, *Cell*, 126(4), 677–689. <https://doi.org/10.1016/j.cell.2006.06.044>

Evans, L. (2010). Partial differential equations (2nd ed.). American Mathematical Society, Providence, R.I.

Dunn G. A., and Heath J.P. 1976. A new hypothesis of contact guidance in tissue cells. *Experimental Cell Research*, 101(1), 1–14. [https://doi.org/10.1016/0014-4827\(76\)90405-5](https://doi.org/10.1016/0014-4827(76)90405-5)

Glimm, J., Li, X. L., Liu, Y., Zhao, N. 1999. Conservative front tracking and level set algorithms. *Proceedings of the National Academy of Sciences* 98, 14198–14201.

Gamsjäger, E., Bidan, C., Fischer, F., Fratzl, P., and Dunlop, J. 2013. Modelling the role of surface stress on the kinetics of tissue growth in confined geometries. *Acta Biomaterialia*, 9(3), 5531–5543. <https://doi.org/10.1016/j.actbio.2012.10.020>

Goldman, R. 2005. Curvature formulas for implicit curves and surfaces. *Computer Aided Geometric Design*, 22(7), 632–658. <https://doi.org/10.1016/j.cagd.2005.06.005>

Goriely A. 2017. The Mathematics and Mechanics of Biological Growth, p. 240–249. Springer Science+Business Media, New York.

Guyot Y., Papantoniou I., Chai Y.C., Van Bael S., Schrooten J., and Geris L. 2014. A computational model for cell/ECM growth on 3D surfaces using the level set method: a bone tissue engineering case study. *Biomechanics and Modeling in Mechanobiology*, 13(6), 1361–1371. <https://doi.org/10.1007/s10237-014-0577-5>

- Haeger A., Wolf K., Zegers M., and Friedl P. 2015. Collective cell migration: guidance principles and hierarchies. *Trends in Cell Biology*, 25(9), 556–566. <https://doi.org/10.1016/j.tcb.2015.06.003>
- Harris, S.E., MacDougall, M., Horn, D., Woodruff, K., Zimmer, S.N., Rebel, V.I., Fajardo, R., Feng, J.Q., Gluhak-Heinrich, J., Harris, M.A., and Abboud Werner, S. 2012. Meox2Cre-mediated disruption of CSF-1 leads to osteopetrosis and osteocyte defects. *Bone*, 50(1) 42–53. <https://doi.org/10.1016/j.bone.2011.09.038>
- Hegarty-Cremer S.G.D. 2020. CBPM_curvature_and_cell_guidance, GitHub repository. https://github.com/SoleneHC/CBPM_curvature_and_cell_guidance
- Hegarty-Cremer, S., Simpson, M., Andersen, T., and Buenzli, P. 2020. Modelling cell guidance and curvature control in evolving biological tissues. BioRxiv. <https://doi.org/10.1101/2020.07.10.197020>
- Hon S., Leung S., and Zhao H. 2014. A cell based particle method for modeling dynamic interfaces. *Journal of Computational Physics*, 272, 279–306. <https://doi.org/10.1016/j.jcp.2014.04.032>
- Ishii, M., Kikuta, J., Shimazu, Y., Meier-Schellersheim, M., and Germain, R.N. 2010. Chemorepulsion by blood S1P regulates osteoclast precursor mobilization and bone remodeling in vivo. *Journal of Experimental Medicine*, 207(13), 2793–2798; <https://doi.org/10.1084/jem.20101474>.
- Jaworski Z.F.G., and Hooper C. 1980. Study of cell kinetics within evolving secondary Haversian systems. *Journal of Anatomy*, 131(1), 91-102.
- Jaworski Z.F.G., Duck B., and Sekaly G. 1981. Kinetics of osteoclasts and their

nuclei in evolving secondary Haversian systems. *Journal of Anatomy*, 133(3), 397–405.

Jin, W., Lo, K., Chou, S., Mccue, S., and Simpson, M. 2018. The role of initial geometry in experimental models of wound closing. *Chemical Engineering Science*, 179(C), 221–226. <https://doi.org/10.1016/j.ces.2018.01.004>

Kollmannsberger, P., Bidan C.M., Dunlop J.W.C., and Fratzl P. 2011. The physics of tissue patterning and extracellular matrix organisation: how cells join forces. *Soft Matter*, 7(20), 9549–9560. <https://doi.org/10.1039/c1sm05588g>

Lassen N., Andersen T., Ploen G., Soe K. Hauge E., Harving S., Eschen G.E.T., and Delaisse J. 2017. Coupling of Bone Resorption and Formation in Real Time: New Knowledge Gained From Human Haversian BMUs. *Journal of Bone and Mineral Research*, 32(7), 1395–1405. <https://doi.org/10.1002/jbmr.309>

Lerebours, C., Buenzli, P., Scheiner, S., and Pivonka, P. 2016. A multi-scale mechanobiological model of bone remodelling predicts site-specific bone loss in the femur during osteoporosis and mechanical disuse. *Biomechanics and Modeling in Mechanobiology*, 15(1), 43–67. <https://doi.org/10.1007/s10237-015-0705-x>

Lerebours, C., Weinkamer, R., Roschger, A., and Buenzli, P.R. 2020. Mineral density differences between femoral cortical bone and trabecular bone are not explained by turnover rate alone. *BioRxiv* <https://doi.org/10.1101/2020.06.08.141036>.

Leung, S. and Zhao, H. 2009. A grid based particle method for moving interface problems. *Journal of Computational Physics*, 228(8), 2993–3024. <https://doi.org/10.1016/j.jcp.2009.01.005>

- Leung, S., Lowengrub, J., and Zhao, H. 2011. A grid based particle method for solving partial differential equations on evolving surfaces and modeling high order geometrical motion. *Journal of Computational Physics*, 230(7), 2540–2561. <https://doi.org/10.1016/j.jcp.2010.12.029>
- Livne A., Bouchbinder E., and Geiger B. 2014. Cell reorientation under cyclic stretching. *Nature Communications*, 5(1), 3938. <https://doi.org/10.1038/ncomms4938>
- Lo C. M., Wang H.B., and Wang Y.L. 2000. Cell movement is guided by the rigidity of the substrate. *Biophysical Journal*, 79(1), 144–152. [https://doi.org/10.1016/S0006-3495\(00\)76279-5](https://doi.org/10.1016/S0006-3495(00)76279-5)
- Lowengrub, J. S., Frieboes H. B., and Cristini V. 2010. Nonlinear modelling of cancer: bridging the gap between cells and tumours. *Nonlinearity*, 23(1), R1–R91. <https://doi.org/10.1088/0951-7715/23/1/R01>
- Maggiano, I.S., Schultz, M., Kierdorf, H., Sosa, T.S., Maggiano, C.M., and Tiesler Blos, V. 2008. Cross-sectional analysis of long bones, occupational activities and long-distance trade of the classic maya from Xcambó—Archaeological and osteological evidence. *American Journal of Physical Anthropology*, 136(4), 470–477. <https://doi.org/10.1002/ajpa.20830>
- Maggiano, C. 2012. Histomorphometry of Humeral Primary Bone: Evaluating the Endosteal Lamellar Pocket as an Indicator of Modeling Drift in Archaeological and Modern Skeletal Samples. The Ohio State University.
- Maini, P., McElwain, D., and Leavesley, D. 2004. Travelling waves in a wound healing assay. *Applied Mathematics Letters*, 17(5), 575–580. <https://doi.org/10.1016/j.aml.2003.01.011>

- Marotti, G., Zallone, A.Z., and Ledda, M. 1976. Number, size and arrangement of osteoblasts in osteons at different stages of formation. Calcification of Tissue Research, 21, 96–101. <https://doi.org/10.1007/BF02546434>
- Marotti, G. 2000. The osteocyte as a wiring transmission system. Journal of Musculoskeletal and Neuronal Interactions, 1(2), 133-136.
- Martin J. Y., Schwartz Z., and Boyan B. D. 1995. Effect of titanium surface roughness on proliferation, differentiation, and protein synthesis of human osteoblast-like cells (MG63). Journal of Biomedical Materials Research, 29(3), 389–401. <https://doi.org/10.1002/jbm.820290314>
- Martin, R. B. 2000. Does osteocyte formation cause the nonlinear refilling of osteons? Bone, 26, 71–78. [https://doi.org/10.1016/S8756-3282\(99\)00242-2](https://doi.org/10.1016/S8756-3282(99)00242-2)
- Martin R., Burr D., and Sharkey N. 2004. Skeletal Tissue Mechanics, p. 32-36. Springer Science+Business Media, New York.
- Mays, S. 2010. The archaeology of human bones. Taylor & Francis; <https://books.google.com.my/books?id=s71ocys3xmUC>
- Mccue, S., Jin, W., Moroney, T., Lo, K., Chou, S., and Simpson, M. 2019. Hole-closing model reveals exponents for nonlinear degenerate diffusivity functions in cell biology. Physica D: Nonlinear Phenomena, 398, 130–140. <https://doi.org/10.1016/j.physd.2019.06.005>
- Murray, J. 2002. Mathematical Biology I. An Introduction (3rd ed.). Springer New York. <https://doi.org/10.1007/b98868>
- Nelson C.M., Jean R.P., Tan J.L., Liu W.F., Sniadecki N.J., Spector A.A., and Chen C.S. 2005. Emergent patterns of growth controlled by multicellular form and mechanics. Proceedings of the National Academy of Sciences of

the United States of America, 102(33), 11594–11599. <https://doi.org/10.1073/pnas.0502575102>

O'Brien, F. 2011. Biomaterials and scaffolds for tissue engineering. Materials Today, 14(3), 88–95. [https://doi.org/10.1016/S1369-7021\(11\)70058-X](https://doi.org/10.1016/S1369-7021(11)70058-X)

Osher, S. and Fedkiw, R. 2003. Level set methods and dynamic implicit surfaces. Springer.

Pazzaglia, U., Congiu, T., Marchese, M., Spagnuolo, F., and Quacci, D. 2012. Morphometry and Patterns of Lamellar Bone in Human Haversian Systems. Anatomical Record: Advances in Integrative Anatomy and Evolutionary Biology, 295(9), 1421–1429. <https://doi.org/10.1002/ar.22535>

Parfitt, A. (1994). Osteonal and hemi-osteonal remodeling: The spatial and temporal framework for signal traffic in adult human bone. Journal of Cellular Biochemistry, 55(3), 273–286. <https://doi.org/10.1002/jcb.240550303>

Pelham R. J. Jr. and Wang Y. L. 1997. Cell locomotion and focal adhesions are regulated by substrate flexibility. Proceedings of the National Academy of Sciences of the United States of America, 94(25), 13661–13665. <https://doi.org/10.1073/pnas.94.25.13661>

Perilli, E., Parkinson, I., and Reynolds, K. 2012. Micro-CT examination of human bone: from biopsies towards the entire organ. Annali dell'Istituto Superiore Di Sanita, 48(1), 75–82. https://doi.org/10.4415/ANN_12_01_13

Polig, E. and Jee, W. 1990. A model of osteon closure in cortical bone. Calcified Tissue International, 47(5), 261–269. <https://doi.org/10.1007/BF02555907>

- Poujade M., Grasland-Mongrain E., and Silberzan P. 2007. Collective migration of an epithelial monolayer in response to a model wound. *Proceedings of the National Academy of Sciences*, 104(41), 15988–15993. <https://doi.org/10.1073/pnas.0705062104>
- Pressley, A. (2010). Elementary Differential Geometry (2nd ed.). Springer, London. <https://doi.org/10.1007/978-1-84882-891-9>
- Redžić D.V. 2001. The operator ∇ in orthogonal curvilinear coordinates. *European Journal of Physics*, 22(6), 595–599. <https://doi.org/10.1088/0143-0807/22/6/304>
- Ripamonti U. and Roden L. 2010. Biomimetics for the induction of bone formation. *Expert Review of Medical Devices*, 7(4), 469–479. <https://doi.org/10.1586/erd.10.17>
- Robling, A. and Stout, S. 1999. Morphology of the Drifting Osteon. *Cells Tissues Organs*, 164(4), 192–204. <https://doi.org/10.1159/000016659>
- Rolli C. G., Nakayama H., and Nakanishi J. 2012. Switchable adhesive substrates: revealing geometry dependence in collective cell behavior. *Biomaterials*, 33(8), 2409–2418. <https://doi.org/10.1016/j.biomaterials.2011.12.012>
- Rumpler M., Woesz A., Dunlop J.W., van Dongen J.T., and Fratzl P. 2008. The effect of geometry on three-dimensional tissue growth. *Journal of the Royal Society, Interface*, 5(27), 1173–1180. <https://doi.org/10.1098/rsif.2008.0064>
- Ryser, M., Nigam, N., and Komarova, S. 2009. Mathematical Modeling of Spatio-Temporal Dynamics of a Single Bone Multicellular Unit. *Journal Of*

Bone And Mineral Research, 24(5), 860–870. <https://doi.org/10.1359/JBMR.081229>

Schrof, S., Varga, P., Galvis, L., Raum, K., and Masic, A. 2014. 3D Raman mapping of the collagen fibril orientation in human osteonal lamellae. Journal of Structural Biology, 187(3), 266–275. <https://doi.org/10.1016/j.jsb.2014.07.001>

Seeman, E. 2008. Modeling and Remodeling: The Cellular Machinery Responsible for the Gain and Loss of Bone’s Material and Structural Strength. In Bilezikian, J., Raisz, L., and Martin, T., Principles of Bone Biology (3rd ed.). Elsevier/Academic Process.

Sethian, J. 1999. Level set methods and fast marching methods: evolving interfaces in computational geometry, fluid mechanics, computer vision, and materials science (2nd ed.). Cambridge, U.K. Cambridge University Press.

Shin, S., Juric, D. 2002. Modeling three-dimensional multiphase flow using a level contour reconstruction method for front tracking without connectivity. Journal of Computational Physics, 180, 427-470.

Skalak, R., Dasgupta, G., Moss, M., Otten, E., Dullemeijer, P., and Vilman, H. 1982. Analytical description of growth. Journal of Theoretical Biology, 94(3), 555–577. [https://doi.org/10.1016/0022-5193\(82\)90301-0](https://doi.org/10.1016/0022-5193(82)90301-0)

Skalak, R., Farrow, D., and Hoger, A. 1997. Kinematics of surface growth. Journal of Mathematical Biology, 35(8), 869–907. <https://doi.org/10.1007/s002850050081>

Smit, B. and Burger, E.H. (2000). Is BMU-Coupling a Strain-Regulated Phenomenon? A Finite Element Analysis. Journal of Bone and Mineral Research, 15(2), 301–307. <https://doi.org/10.1359/jbmr.2000.15.2.301>

- Stone, H. 1990. A simple derivation of the time-dependent convective-diffusion equation for surfactant transport along a deforming interface. *Physics of Fluids A: Fluid Dynamics*, 2(1), 111–112. <https://doi.org/10.1063/1.857686>
- Trepat, X., Deng, L., An, S.S., Navajas, D., Tschumperlin, D.J., Gerthoffer, W.T., Butler, J.P., and Fredberg, J.J. 2007. Universal physical responses to stretch in the living cell. *Nature*, 447(7144), 592–595. <https://doi.org/10.1038/nature05824>
- Tryggvason, G., Bunner, B., Esmaeeli, A., Juric, D., Al-Rawahi, N., Tauber, W., Hans, J., Nas, S., and Jan, Y.-J. 2001. A front-tracking method for the computations of multiphase flow. *Journal of Computational Physics*, 169, 708–759.
- Turner, C.H., Forwood, M.R., Otter, M.W. 1994. Mechanotransduction in bone: do bone cells act as sensors of fluid flow? *FASEB Journal*, 8, 875–878.
- Wong, H., Rumschitzki, D., and Maldarelli, C. 1996. On the surfactant mass balance at a deforming fluid interface. *Physics of Fluids*, 8(11), 3203–3204. <https://doi.org/10.1063/1.869098>
- Wu, A.C., Morrison, N.A., Kelly, W.L., and Forwood, M.R. 2013. MCP-1 expression is specifically regulated during activation of skeletal repair and remodeling, *Calcified Tissue International*, 92(6), 566–575.
- Yang, J., Shah, R. Robling, A.G., Templeton, E. Yang, H., Tracey, K.J., and Bidwell, J.P. HMGB1 is a bone-active cytokine. *Journal of Cellular Physiology*, 214(3), 730–739. <https://doi.org/10.1002/jcp.21268>
- Xu, J., and Zhao, H. 2003. An Eulerian Formulation for Solving Partial Differential Equations Along a Moving Interface. *Journal of Scientific Computing*, 19(1), 573–594. <https://doi.org/10.1023/A:1025336916176>